

# PatchEX: High-Quality Real-Time Temporal Supersampling through Patch-based Parallel Extrapolation

AKANKSHA DIXIT, Electrical Engineering, Indian Institute of Technology Delhi, India

SMRUTI R. SARANGI, Electrical Engineering, Indian Institute of Technology Delhi, India

High-refresh rate displays have become very popular in recent years due to the need for superior visual quality in gaming, professional displays and specialized applications like medical imaging. However, high-refresh rate displays alone do not guarantee a superior visual experience; the GPU needs to render frames at a matching rate. Otherwise, we observe disconcerting visual artifacts such as screen tearing and stuttering. Temporal supersampling is an effective technique to increase frame rates by predicting new frames from other rendered frames. There are two methods in this space: interpolation and extrapolation. Interpolation-based methods provide good image quality at the cost of a higher latency because they also require the next rendered frame. On the other hand, extrapolation methods are much faster at the cost of quality. This paper introduces *PatchEX*, a novel frame extrapolation method that aims to provide the quality of interpolation at the speed of extrapolation. It smartly partitions the extrapolation task into sub-tasks and executes them in parallel to improve both quality and latency. It then uses a patch-based inpainting method and a custom shadow prediction approach to fuse the generated sub-frames. This approach significantly reduces the overall latency while maintaining the quality of the output. Our results demonstrate that *PatchEX* achieves a 65.29% and 48.46% improvement in PSNR over the latest extrapolation methods ExtraNet and ExtraSS, respectively, while being 6× and 2× faster, respectively.

CCS Concepts: • **Computer systems organization** → **Real-time systems**; • **Computing methodologies** → **Rendering**; **Machine learning**.

Additional Key Words and Phrases: Extrapolation, Warping, G-buffer, Shadow Map

## ACM Reference Format:

Akanksha Dixit and Smruti R. Sarangi. 2024. *PatchEX*: High-Quality Real-Time Temporal Supersampling through Patch-based Parallel Extrapolation. 1, 1 (July 2024), 36 pages. <https://doi.org/XXXXXXXX.XXXXXXX>

## 1 INTRODUCTION

In the last few years, there has been a significant growth in the demand for high-refresh rate displays. Refresh rates have reached 360 Hz for major monitor brands. Dell's latest monitors can support refresh rates of up to 500 Hz [Technologies 2023]. This surge is driven by the need for enhanced visual quality in various market segments such as gaming, professional displays (used in fields like finance and e-sports) and specialized applications such as medical imaging and scientific visualization [Gembler et al. 2018; Huhti 2019; Murakami et al. 2021]. The global gaming monitor market alone was valued at around USD 9.51 billion in 2022 and is projected to grow to approximately USD 16.04 billion by 2030 with a compound annual growth rate (CAGR) of 6.76% between 2023 and 2030 [gam 2023]. The reason for this trend is because low-refresh rate displays may exhibit various visual artifacts such as judder (non-continuous motion perception) and motion blur during high-speed motion [Han

---

Authors' addresses: Akanksha Dixit, Electrical Engineering, Indian Institute of Technology Delhi, New Delhi, India, [Akanksha.Dixit@ee.iitd.ac.in](mailto:Akanksha.Dixit@ee.iitd.ac.in); Smruti R. Sarangi, Electrical Engineering, Indian Institute of Technology Delhi, New Delhi, India, [srsarangi@cse.iitd.ac.in](mailto:srsarangi@cse.iitd.ac.in).

---

Permission to make digital or hard copies of all or part of this work for personal or classroom use is granted without fee provided that copies are not made or distributed for profit or commercial advantage and that copies bear this notice and the full citation on the first page. Copyrights for components of this work owned by others than the author(s) must be honored. Abstracting with credit is permitted. To copy otherwise, or republish, to post on servers or to redistribute to lists, requires prior specific permission and/or a fee. Request permissions from [permissions@acm.org](mailto:permissions@acm.org).

© 2024 Copyright held by the owner/author(s). Publication rights licensed to ACM.

ACM XXXX-XXXX/2024/7-ART

<https://doi.org/XXXXXXXX.XXXXXXX>

et al. 2022]. High-frequency displays thus aim to deliver a smooth and seamless experience by eliminating these artifacts.

**GPU is the bottleneck:** It is crucial to acknowledge that having high-frequency displays alone may not always guarantee smooth performance unless the frame rendering rate matches the refresh rate. When the rendering rate is lower than the refresh rate, visual artifacts such as screen tearing and stuttering can occur [Denes et al. 2020]. Therefore, it is essential for the GPU to render frames at a matching rate, which is seldom feasible. As graphics engineers continue to incorporate increasingly complex effects into graphics applications to enhance realism, the rendering process becomes more intricate and time consuming. Several studies have shown the variation in the rendering rate and its impact on the quality of experience for users [Liu et al. 2023; Sabet et al. 2020; Xu and Claypool 2024]. This necessitates the exploration of strategies to upsample the rendering rate in real-time even for the latest consumer-grade GPUs.

**Temporal supersampling fills in frames missed by the GPU:** One of the most impactful approaches to increase the frame rate is *temporal supersampling*, which involves predicting frames using information from the next and previously rendered frames [Guo et al. 2021; He et al. 2024; Niklaus and Liu 2020; Wu et al. 2023a,b; Zhang et al. 2023]. The core concept here is that since rendering new frames is time-consuming, we can expedite the process by predicting new frames from previously rendered ones or the next frame (in temporal sequence) and interleave the frames at the display device. This boosts the frame rate and achieves rate matching. For temporal supersampling to be effective, it is important to ensure that the prediction latency is shorter than the rendering time and that the predicted frame is of acceptable quality. Particularly in real-time systems like virtual reality applications and games, minimizing latency and ensuring good quality are of utmost importance.

**Interpolation: high quality, high latency | Extrapolation: low quality, low latency:** In the field of temporal supersampling, two primary methodologies exist: *interpolation* [Niklaus and Liu 2020; Wu et al. 2023b; Zhang et al. 2023] and *extrapolation* [Guo et al. 2021; He et al. 2024; Wu et al. 2023a]. As their names imply, interpolation predicts a frame using both past and future frames, whereas extrapolation creates a new frame by utilizing only the past few frames. Fig. 1 shows the performance of a few recent works in terms of quality and latency. It is evident that interpolation yields superior quality but comes with a higher latency (**almost 14 ms**, not suitable for a 90 Hz display), whereas extrapolation offers lower latency at the expense of inferior quality. This is because interpolation takes into account both past and future frames (see Section 2.2 for more details).

Therefore, the challenge is quite clear:

**Match the quality of interpolation with the performance of extrapolation.**

Note that interpolation introduces an inherent latency by holding an already rendered frame for a refresh interval before displaying it. This is something that the human visual system can easily detect. We tested an interpolation algorithm on a 360-Hz display and ourselves did not find the quality of the images very appealing. We thus propose an extrapolation-based approach that does not incur this overhead. Given that historically such algorithms produced low-quality outputs, real-time extrapolation is a less explored area. As per our knowledge, there are only three major works that specifically address this: ExtraNet [Guo et al. 2021], ExtraSS [Wu et al. 2023a] and STSS [He et al. 2024]. These methods use a warping algorithm[] that transforms the frame using a motion vector. Warping algorithms often lead to invalid pixels and holes in certain regions and incorrect shading in other regions. Various approaches such as using neural networks have been employed to rectify these issues. They use the information stored in G-buffers – these are data structures in the rendering engine that store different properties of a scene such as the scene depth, roughness, etc.. Despite these efforts, none of the methods have produced satisfactory results in complex dynamic environments with multiple characters and

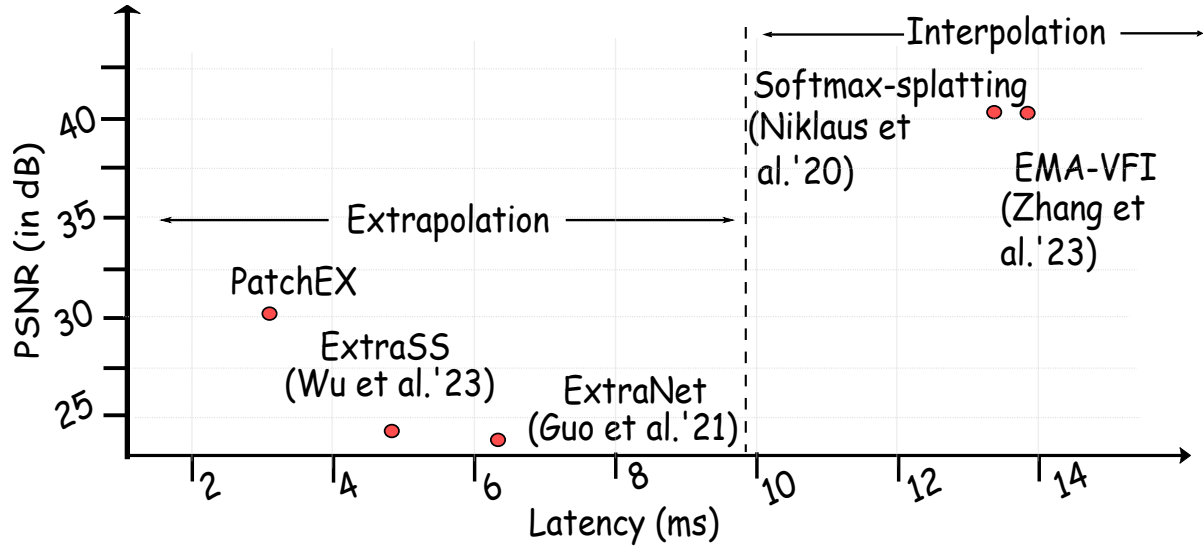


Fig. 1. The solution space for temporal supersampling. Each solution is run on an NVIDIA RTX 4090 GPU. The detailed system configuration is shown in Table 4.

lighting sources. Even though baseline extrapolation methods are fast, the moment neural networks are added, they become very slow.

**Partition and parallelize:** In this paper, we introduce *PatchEX*, a novel approach that is significantly different from prior frame extrapolation methods. Our methodology involves smartly partitioning the extrapolation task into sub-tasks and executing them in parallel. The key idea is that we take the warped frame as an initial prediction for extrapolation. Subsequently, we divide the frame extrapolation task into two primary sub-tasks: fixing invalid pixels in the warped frame (inpainting) and ensuring proper shadowing in the warped frame. *PatchEX* proposes independent and simultaneous handling of shadows and inpainting tasks. To achieve this, we remove the shadow information from the frame and store it in a separate buffer.

The first subtask uses a patch-based inpainting method [Demir and Unal 2018; Xu et al. 2021] to fix the warped frame. Unlike previous inpainting approaches, we segment the entire frame (without shadows) into three distinct patches/parts after taking into account the idiosyncrasies of the human vision system (known as *foveated segmentation*) [Björkman and Eklundh 2005]. Each patch is subsequently processed in parallel by separate neural networks that are small in size. This approach bears a resemblance to classical foveated rendering [Guenther et al. 2012; Meng et al. 2020a], which aims to optimize rendering efficiency without compromising visual fidelity. This strategic parallelism drastically reduces the overall latency. Furthermore, feeding smaller patches to the inpainting networks reduces the inference time.

To handle shadows (second subtask), we create a custom blueprint class in the Unreal Engine (UE) [Games 2023b] to extract the shadow map/mask. Using this mask, we predict shadows for the inpainted frame. After the image is inpainted and shadows are predicted, we merge them to produce the final extrapolated frame.

Currently, we lack large-scale publicly available datasets or workloads for characterizing the real-time rendering of graphics applications. To address this, we create a dataset by downloading model and scene files from *Epic Games* [Games 2023a] and rendering them using *Unreal Engine* (v5.1) [Games 2023b]. Our dataset includes

multiple animation sequences featuring a diversity of characters, lighting effects, background scenes and camera motions.

To summarize, our primary contributions are as follows:

- ❶ The first innovation is that we generate a warped frame very quickly to guide the process of accurate frame generation.
- ❷ Henceforth, the first subtask partitions the warped frame (devoid of shadows) into three different partitions based on the *perceived distance* from the eye. These are rendered differently using different kinds of neural networks.
- ❸ The inpainting method proposed in step (2) runs in parallel for the three kinds of patches (partitions).
- ❹ We meticulously curated a comprehensive dataset featuring a wide range of animation sequences encompassing diverse characters, backgrounds, lighting settings and camera movements.
- ❺ *PatchEX* shows an improvement of 65.29% and 48.46% in the PSNR (peak signal-to-noise ratio) compared to the two most recent extrapolation methods, *ExtraNet* and *ExtraSS*, respectively.
- ❻ The proposed inpainting network is 6× and 2× faster than the nearest competing works *ExtraNet* and *ExtraSS*, respectively.

The paper is organized as follows. Section 2 describes the background and related work in the area of temporal supersampling. Section 3 characterizes the datasets and provides the motivation for the proposed approach. Section 4 presents the methodology in detail. The implementation details are provided in Section 5. Section 6 shows the experimental results. We finally conclude in Section 7.

## 2 BACKGROUND AND RELATED WORK

### 2.1 QoE Requirements of Graphics Applications

Graphics applications need to provide a certain Quality of Experience (QoE) to ensure that users get the best possible experience. Some of the key QoE requirements are: ❶ **Low latency or high frame rate:** This is important to ensure that the user sees the effect on the screen as soon as possible after providing an input – this creates a responsive environment that immerses the user in the virtual world. ❷ **High visual quality:** The rendered frames should be free of visual artifacts such as ghosting, stuttering, motion blurring and screen tearing. ❸ **Realism:** The frames should have advanced lighting effects, shadows, and reflections such that the virtual environment appears realistic. This work aims to provide all these properties with the available hardware resources of a consumer-grade GPU.

### 2.2 Temporal Supersampling in Frame Rendering

Recent works primarily focus on ❶ predicting new frames using interpolation [Andreev 2010; Herzog et al. 2010; Nehab et al. 2007] and ❷ generating new frames using extrapolation [Guo et al. 2021] to increase the frame rate. We present a brief comparison of related work in Table 2.

As mentioned in Section 1, apart from the latency of the algorithm used for interpolation, there is an additional latency incurred here because *interpolation* predicts frames between two already rendered neighboring frames. We thus need to wait more. In contrast, extrapolation-based methods predict frames solely based on past frames. The difference can be observed in Fig. 2. Both processes double the frame rate by generating a new frame after each rendered frame. However, interpolation increases the display or presentation latency. In the figure, the presentation latency is the delay between the completion of a frame’s rendering and its actual display on the screen.

The mathematical formulae for the presentation latency of interpolation and extrapolation, respectively, are shown in Table 1 (keep referring to Fig. 2). The first assumption is that the rendering time for every frame is greater than one refresh interval  $D$  (in the super-sampled case). If this is not the case, then there is no

Table 1. Presentation latency for interpolation and extrapolation

$\forall i, R_i > D$	assumption
$P_i = 3D - R_i$ $R_i + I \leq 2D$	interpolation
$P_i = 0$ $R_{i+1} + E \leq 2D$	extrapolation

need to interpolate or extrapolate in the first place. It is further assumed that the rendering duration plus the interpolation/extrapolation time does not exceed two refresh intervals  $2D$ . We observe in Fig. 2 that if the sum exceeds  $2D$ , then the interpolated frame will simply not be ready by the time that it needs to be displayed. The assumption here is that we are supersampling by a factor of  $2\times$ . We will have similar formulae for other super-sampling ratios. Our algorithm per se is not constrained by this choice. The choice of 2 in this example is for the purpose of better explanation.

$P_i$  and  $R_i$  denote the presentation latency and rendering latency for the  $i^{th}$  frame, respectively.  $D$  represents the refresh interval.  $E$  is the latency associated with generating an extrapolated frame (the  $(i + 0.5)_{th}$  frame) based on frame  $F_i$ , while  $I$  is the latency for generating an interpolated frame using frames  $F_i$  and  $F_{i+1}$ . If we consider a 90 Hz display, the refresh interval  $D$  is 11.11 ms. Hence, the presentation latency  $P_i$  for interpolation falls within the range of 11.11 ms to 22.22 ms, which is considerably larger than the latency for extrapolation, which is 0 (in a system without slack).

This latency introduced by interpolation significantly affects the user experience due to the human visual system’s acute sensitivity to delays. The concept of the just noticeable delay (JND) [Jerald 2009] underscores this sensitivity, indicating that humans can normally detect delays as low as 3-5 ms with the threshold for gamers and active young people being even lower. It needs to be less than 1 ms in the case of Head-Mounted Displays (HMDs) [Alja’Afreh 2021; Jerald and Whitton 2009]. **Given these factors, the latency introduced by interpolation (11.11 ms to 22.22 ms) can easily exceed the JND thresholds, leading to perceptible delays and compromising the quality of the viewing experience.**

Table 2. A comparison of related work

Year	Work	Coherence Exploited	Method Used	ML-based	Real-time	Upsampling Domain	Upsampling Factor
2007	Nehab et al. [Nehab et al. 2007]	Spatio-temporal	Interpolation	×	×	Temporal	
2010	Andreev et al. [Andreev 2010]	Temporal	Interpolation	×	×	Temporal	x to 60
2010	Herzog et al. [Herzog et al. 2010]	Spatio-temporal	Interpolation	×	×	Temporal	
2012	Bowles et al. [Bowles et al. 2012]	Temporal	Interpolation	×	×	Temporal	
2018	SAS [Mueller et al. 2018]	Temporal	Interpolation	×	×	Temporal	x to 120
2020	Softmax-splatting [Niklaus and Liu 2020]	Temporal	Interpolation	✓	×	Temporal	up to 2
2021	ExtraNet [Guo et al. 2021]	Temporal	Extrapolation	✓	✓	Temporal	up to $2\times$
2022	DLSS 3 [Burnes and C Lin 2023]	Spatio-temporal	Interpolation	✓	✓	Temporal	up to $4\times$
2023	EMA-VFI [Zhang et al. 2023]	Temporal	Interpolation	✓	×	Temporal	up to $4\times$
2023	ExtraSS [Wu et al. 2023a]	Temporal	Extrapolation	✓	✓	Spatio-temporal	up to $2\times$
2024	STSS [He et al. 2024]	Temporal	Extrapolation	✓	✓	Spatio-temporal	$2\times$
<b>2024</b>	<b>Ours</b>	<b>Temporal</b>	<b>Extrapolation</b>	✓	✓	<b>Temporal</b>	<b><math>2\times</math></b>

**2.2.1 Interpolation.** Early temporal supersampling-based methods [Nehab et al. 2007] use optical flow-guided interpolation, but they produce subpar results when the scene contains areas visible in the current frame but not in

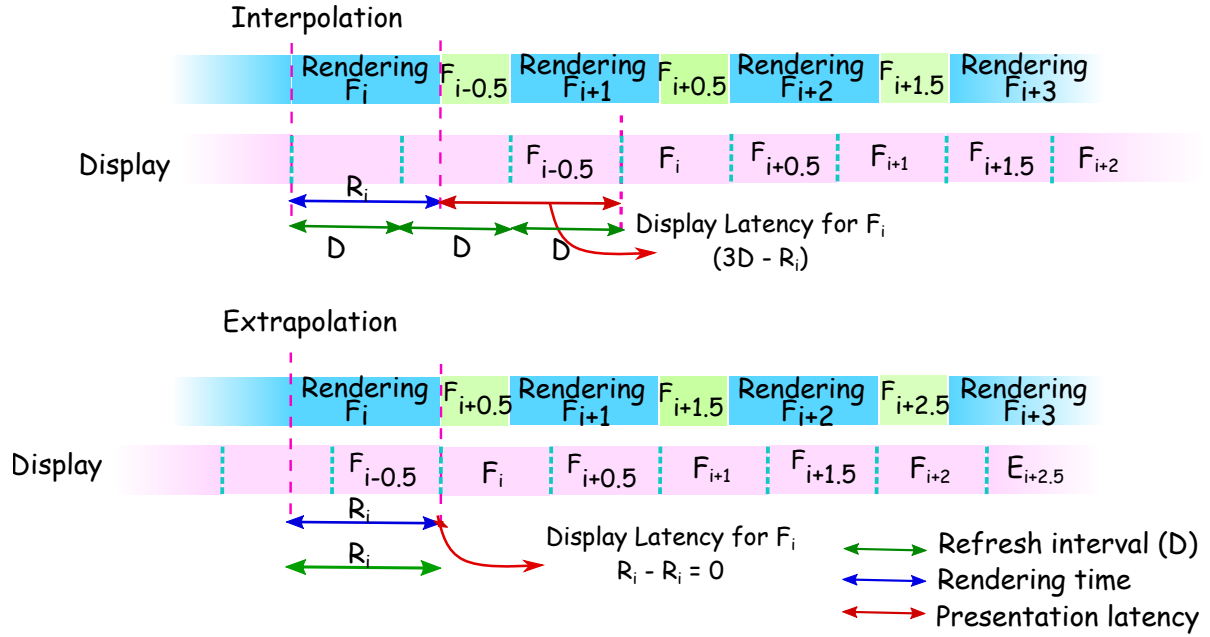


Fig. 2. Interpolation and extrapolation explained.  $F_i$  is the rendered frame.  $R$  and  $D$  represent the rendering time and refresh latency, respectively.

the previous one. Although Bowles et al. [Bowles et al. 2012] proposed to fix this using an iterative method called fixed point iteration (FPI), this did not provide satisfactory results. To handle this case, various works [Burnes and C Lin 2023; Mueller et al. 2018] propose a bidirectional reprojection method that temporally upsamples frames by reusing data from both the backward and forward temporal directions. For example, NVIDIA’s latest DLSS3 engine does this using an optical flow generator, a frame generator and a supersampling network that is AI-accelerated and integrated into its latest GPU architecture (Ada Lovelace [Burnes and C Lin 2023]). This approach increases the frame rate but also leads to an increased input latency that users can easily perceive (verified in the lab and reported in the literature[]). Since our approach is not based on optical flow fields, it does not require future frames to predict a new frame. Other methods, such as caching techniques [Nehab et al. 2007] and dividing frames into slow-moving and fast-moving parts and rendering each part at a different rate [Andreev 2010] have also been proposed but they increase the time needed to construct a frame significantly. Recently, DNN-based solutions [Niklaus and Liu 2020; Zhang et al. 2023] have also been proposed to produce a high-quality interpolated frame. However, this increases the latency of the interpolation process due to the complex structure of neural networks.

**2.2.2 Extrapolation.** This is a very sparse area of research. The prominent works that we are aware of are ExtraNet [Guo et al. 2021], ExtraSS [Wu et al. 2023a] and STSS [He et al. 2024]. To predict a new frame, all of these works first propose a warping algorithm that helps generate a warped frame that serves as an initial prediction. However, the warped frame may have invalid pixels or holes in disoccluded regions where the temporal information is not available; this leads to incorrect shading (shadows and reflections) in other regions. To fix the holes, they use a neural network similar to an image inpainting network [Bertalmio et al. 2000; Guillemot and Le Meur 2013]. However, it may not be sufficient in cases where the shading information changes dynamically

over time. To handle this, ExtraNet [Guo et al. 2021] uses a history encoder to learn the shading pattern from the previous few frames and fix that in the warped frame. This approach works well when the lighting conditions change slowly over time.

On the other hand, STSS [He et al. 2024] uses light source information along with a history encoder. Whereas, ExtraSS [Wu et al. 2023a] introduces a new warping method to minimize the presence of invalid pixels in the warped frame. Their technique utilizes G-buffers' information for the warping process. The G-buffer is a set of render targets that store various properties of a scene during the rendering process. It then uses a lightweight neural network to fine-tune the shading. Sadly, none of these works produce a satisfactory result in a complex dynamic environment with numerous characters and lighting sources. Apart from the quality issue, the latency of these methods due to their heavy neural networks is significant. Note that the latest work ExtraNet [Guo et al. 2021] is a pure temporal supersampling approach, while the remaining two [He et al. 2024; Wu et al. 2023a] propose a joint neural network for supersampling in both temporal and spatial domains. We focus our research solely on the temporal domain. We can use a complementary spatial supersampling method if there is a need to increase the resolution of our generated images.

### 2.3 Image Warping

Image warping is a technique that changes the shape or appearance of an image by applying a spatial transformation. This transformation can include rotation, scaling, translation or other complex deformations. Recent works use motion vector-based warping [Guo et al. 2021; He et al. 2024; Wu et al. 2023a], where motion vectors encode the displacement of blocks or regions across frames. These vectors consist of horizontal and vertical components that indicate the amount of movement in the  $x$  and  $y$  directions, respectively. There are two types of warping techniques: forward warping and backward warping [Lee et al. 2018; Shimizu et al. 2022].

In forward warping, each pixel in the frame that needs to be warped (the source frame) is directly mapped to a corresponding position in the warped frame using the motion information. On the other hand, backward warping involves traversing each pixel in the target frame and finding its corresponding position in the source frame by applying the inverse transformation [Zhang et al. 2003]. Each algorithm has its pros and cons. Forward warping is simpler than backward warping since it directly uses the transformation function to map source pixels to the target. However, this direct transformation may result in overlaps because multiple source pixels may be mapped to the same target pixel. Additionally, forward warping can create empty spaces or holes in the target frame if all the target pixels do not receive a mapped value from the source image. In backward warping, although it is possible that a target pixel might not find a corresponding source pixel, resulting in holes, these holes are filled using the values of the nearest source pixels. Therefore, backward warping produces better quality images as compared to forward warping because it ensures that every pixel in the target image is assigned a value, avoiding gaps or holes. Forward warping, on the other hand, handles gaps through post-processing interpolation after the warping is completed [Guo et al. 2021; Lee et al. 2018].

Using motion vectors results in residual frames or trails of moving objects in the warped frame, also known as the *ghosting* effect. This occurs because motion vectors store pixel displacements between consecutive frames but fail to provide information about disoccluded regions. Traditional algorithms in this space propose to use the same pixel values from previous frames in these regions, resulting in ghosting. To address this issue, Zeng et al. [Zeng et al. 2021] have proposed a method for generating occlusion motion vectors. These vectors calculate displacements in disoccluded regions as displacements of nearby regions in the previous frame. But it still fails when the background becomes complex. To overcome this challenge, Wu et al. [Wu et al. 2023a] introduced a novel technique called G-buffer-guided warping. This method utilizes a joint bilateral filter that computes the warped pixels, enabling more accurate and reliable tracking of complex movements. Specifically, it considers a large area of pixels near the warped pixel and uses weighted G-buffers' values to blend them to form the warped

pixel. As a result, G-buffer-guided warping has emerged as an effective warping method. Hence, we adopt this technique to generate inputs for our inpainting network.

**2.3.1 Structure of a G-Buffer.** In the Unreal Engine, a G-buffer (Geometry Buffer) is a set of render targets that store various pieces of information about the geometry such as the world normal, base color, roughness, textures, etc. During the lighting calculation phase, the Unreal Engine samples these buffers to determine the final shading of the scene. The G-buffer generally consists of several textures in the standard RGBA format. However, Unreal optimizes the performance by packing these attributes into fewer textures by combining different channels. The exact composition of the G-buffer can vary with the number of channels. A common example is a five-texture *GBuffer*, which consists of five buffers: *A* through *E* (refer to Table 3). Specifically, *GBufferA.rgb* stores the base color with *transparency* filling the alpha channel. *GBufferB.rgba* stores the properties – metallic, specular and roughness – and the scene depth. *GBufferC.rgb* stores the world normal (WN) vector with *GBufferAO* (AO: Ambient Occlusion) filling the alpha channel. *GBufferD* is dedicated to custom data (stencil buffer) and *GBufferE* is for precomputed shadow factors.

<b>G-Buffer</b>	<b>R</b>	<b>G</b>	<b>B</b>	<b>A</b>
<b>A</b>	Base Color (R)	Base Color (G)	Base Color (B)	Transparency
<b>B</b>	Metallic	Specular	Roughness	Depth
<b>C</b>	WN (X)	WN (Y)	WN (Z)	AO
<b>D</b>	Custom data (stencil buffer)			
<b>E</b>	Precomputed shadow factors			

Table 3. G-buffer layout in Unreal

## 2.4 Foreground Bias Effect in Human Vision

The human visual system is an incredibly complex and sophisticated mechanism responsible for perceiving and interpreting visual information. The process of generating new frames can be challenging due to the intricate nature of this system, which is highly sensitive to even the slightest input latency and may experience jitter [Ng et al. 2012; Weier et al. 2017]. However, certain characteristics of the human vision system can be leveraged to optimize the frame generation process. One of these characteristics is known as “*foreground bias*” or “*foreground dominance*” [Fernandes and Castelhana 2021]. This phenomenon occurs because the human visual system tends to focus more on objects in the foreground than those in the background. The primary cause is that the foreground objects are usually closer to the observer than background elements, this leads to a greater disparity in the retinal image size. It also provides stronger depth cues (refer to Fig. 6). Our visual system is highly sensitive to depth cues, which contribute to the perceptual salience of foreground objects compared to background environments. The same effect in game engines like Unity and Unreal Engine are emulated using a technique known as *Perspective Projection* [Toth et al. 2016] making far-away objects appear smaller and fainter than foreground objects.

The foreground bias effect can be used to our advantage by extrapolating foreground interactions more efficiently since artifacts are more noticeable in the foreground as compared to the background.

## 3 CHARACTERIZATION AND MOTIVATION

In this section, we begin by presenting the benchmarks used in our experiments. Next, we evaluate the frame rendering times and pinpoint the factors contributing to the latency overhead and frame rate variability. We then



Table 4. Platform Configuration

Parameter	Type/Value
CPU	Intel®Xeon®Gold 6226R @ 2.90GHz
# CPU cores	64
RAM	256 GB
L1, L2, and L3 cache	2 MB, 32 MB, and 44 MB
GPU	NVIDIA RTX™4080
GPU memory	16 GB
#CUDA cores	9728
Game engine	Unreal Engine v5.1

Table 5. Graphics benchmarks

Abbr.	Name	Res.	Graphics API	Engine	Game Engine
<i>PR</i>	City Park	360p	DX12	Epic Games	UE
<i>WT</i>	Western Town	360p	DX12	Epic Games	UE
<i>RF</i>	Redwood Forest	360p	DX12	Epic Games	UE
<i>CM</i>	Cemetery	360p	DX12	Epic Games	UE
<i>BR</i>	Bridge	360p	DX12	Epic Games	UE
<i>DW</i>	Downtown West	360p	DX12	Epic Games	UE
<i>TC</i>	Tennis Court	360p	DX12	Epic Games	UE
<i>LB</i>	Lab	360p	DX12	Epic Games	UE
<i>BK</i>	Bunker	360p	DX12	Epic Games	UE
<i>TR</i>	Tropical	360p	DX12	Epic Games	UE
<i>VL</i>	Village	360p	DX12	Epic Games	UE
<i>TN</i>	Town	360p	DX12	Epic Games	UE
<i>SL</i>	Slum	360p	DX12	Epic Games	UE

UE: Unreal Engine, DX: DirectX

demonstrate how any frame can be segmented into three distinct regions with varying levels of detail, aligning with the viewer’s perception of changes within each region. This *strategic segmentation forms a pivotal element of our approach*. Finally, we address the challenges inherent in the extrapolation process.

### 3.1 Overview of the Datasets

We render our datasets using Unreal Engine 5 (UE5 v5.1) on an NVIDIA RTX series GPU with the Ada Lovelace architecture. The detailed configuration is shown in Table 4. To create our animation sequences, we downloaded Unreal scene files from the UE Marketplace [Games 2023a]. We further complicated it by integrating animations with characters from Mixamo [mix 2024] into the background scenes to generate various animation sequences.

To ensure the generalizability of our approach, we aimed to create a wide-ranging dataset. We gathered 13 background environments from the UE Marketplace, each with unique artistic styles and complexities. In these environments, we randomly inserted over 20 different characters along with 30 animation sequences, ranging from simple walks to complex hip-hop dances. We then selected good viewpoints and created camera paths to follow the main animation character for each animation sequence to create a variety of sequences. In this regard, we followed a method used to create datasets in recent works [Li et al. 2022; Shugrina et al. 2019]. Sample scenes of a few applications are shown in Fig. 3.



Fig. 3. Example views from a few sample scenes

### 3.2 Variation in the Frame Rate

As highlighted in Section 1, visual artifacts such as screen tearing and judder can occur even with a high refresh rate display. This is often due to the irregular delivery of frames from the GPU. This section delves deeper into the variability of frame rates in real-world applications. We conducted extensive experiments, measuring the total rendering time for each frame in a scene with a single dynamic object. By plotting these values over time (see Fig. 4), we observe significant fluctuations in the FPS (frames per second) with some frames taking considerably longer to render. The average FPS is almost 29, while the standard deviation is 6.6, indicating that the FPS values show considerable variability or spread around the mean. This inconsistency leads to noticeable flickering, distracting viewers and degrading image quality. Our findings underscore the necessity of temporal supersampling to stabilize the frame rate, aligning it more closely with the display's refresh rate, and thus ensuring high-quality, flicker-free images.

When a frame is being rendered, it passes through a series of steps that form the rendering pipeline. To better understand the reasons behind the high rendering time and variability, we conduct a detailed analysis of the pipeline. We identify the top ten high-latency steps that cause delays and plot them in Fig. 5. The plot shows that the ShadowDepths, BasePass, PrePass and ShadowProjections steps are the most time-consuming ones. These steps involve complex calculations and require significant computing resources, which can result in high rendering times.

#### 3.2.1: Insight

For a real-world application, we achieve an average FPS of 29 with a standard deviation of 6.6. This highlights the necessity of using temporal supersampling to ensure a stable frame rate.

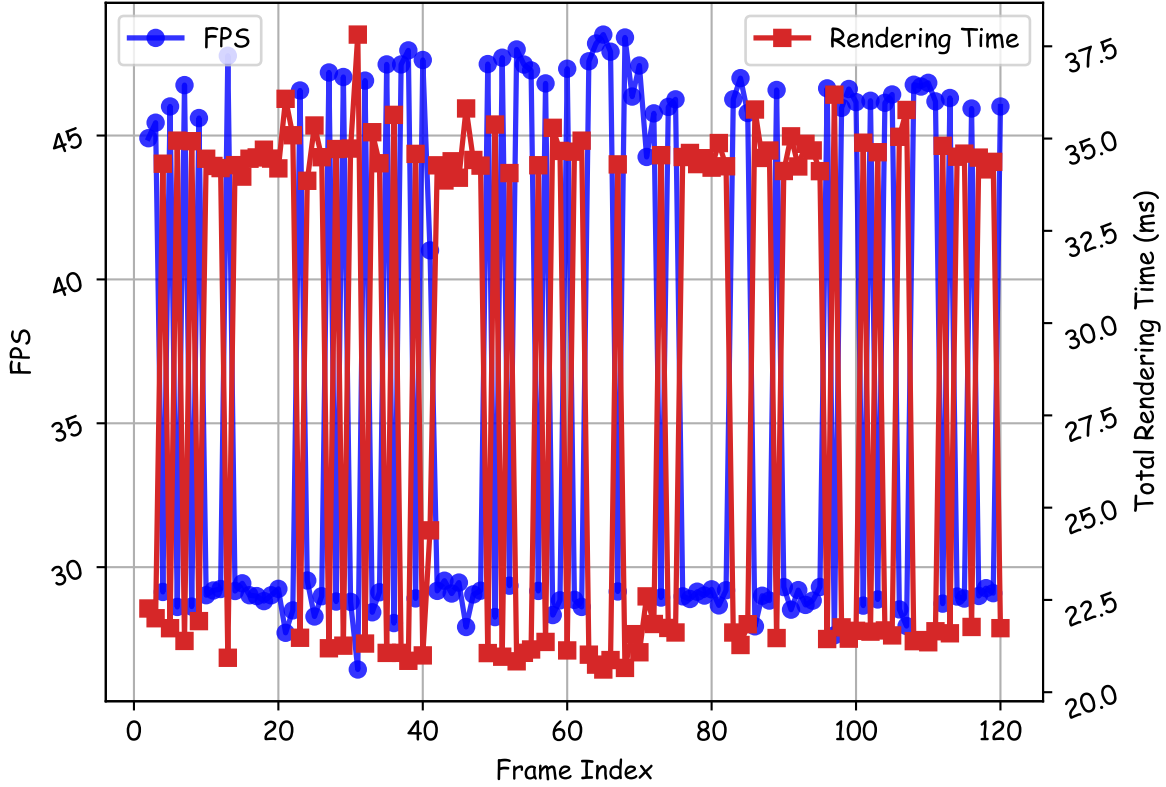


Fig. 4. Variation in the total rendering time

### 3.3 Foveated Segmentation

As mentioned in Section 2.4, the foreground bias effect can be used to our advantage by extrapolating foreground interactions more efficiently since artifacts are more noticeable in the foreground as compared to the background. To achieve this, we segment a frame into two parts: foreground and background. This is known as foveated segmentation [Björkman and Eklundh 2005]. We can then use different extrapolation algorithms for each part and blend the outputs. However, there is another effect that complicates this simple division of the frame. This effect is known as the near-object effect [Meng et al. 2020b], which means that changes in the pixels in the background around the foreground objects are more noticeable than those further away from the foreground objects. Hence, similar to Coterie [Meng et al. 2020b], we, too, divide the entire frame into three regions: FI (foreground interactions), Near-BE (near background environment) and Far-BE (refer Fig. 6). We propose a *novel algorithm* in this space. The near and far background environments are separated by a rectangular boundary of width and height,  $w$  and  $h$ , respectively. In Section 5.2, we will delve into the selection process for determining the width ( $w$ ) and height ( $h$ ).

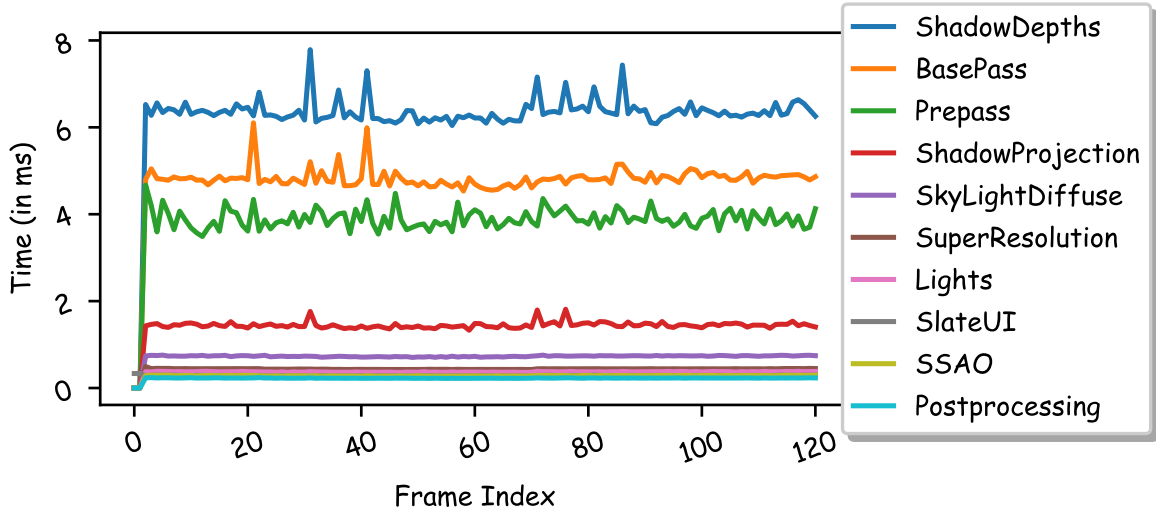


Fig. 5. Top 10 high-latency steps in the rendering process



Fig. 6. Types of objects in a frame

## 3.3.1: Insight

The extrapolation can be more efficiently performed by exploiting the fact that humans perceive different parts of an image with varying levels of sensitivity.

Aspect Ratio	Resolution	Name	# Pixels
4:3	320 x 240	QVGA	0.0768
	640 x 480	VGA	0.3072
	800 x 600	SVGA	0.4800
	1024 x 768	XGA	0.7864
	1280 x 960	SXGA-	1.2288
	1400 x 1050	SXGA+	1.4700
	1600 x 1200	UXGA	1.9200
16:9	2048 x 1536	QXGA	3.1457
	640 x 360	nHD	0.2304
	854 x 480	FWVGA	0.4099
	1280 x 720	HD or 720p	0.9216
	1600 x 900	HD+	1.4400
	1920 x 1080	Full HD or 1080p	2.0736
	2560 x 1440	Quad HD or 1440p	3.6864
3840 x 2160	4K or UHD	8.2944	

Table 6. Common resolutions for 4:3 and 16:9 aspect ratios with pixel counts (in millions)

## 3.4 Latency of the Inpainting Task

As mentioned in Section 1, we propose to segment the warped frame into three distinct patches. Each patch is subsequently inpainted in parallel by separate neural networks. This approach leverages the benefits of parallel processing, which is advantageous from the point of view of performance, especially when the task execution time is a superlinear function of the task size. In other words, if the inpainting latency increases super-linearly with the input frame size, we can naturally justify frame splitting and parallelization.

To illustrate this, we inpaint frames rendered at various resolutions (refer to Table 6) and compute their latencies. The results, shown in Figure 7, indicate that the relationship between the frame size (total number of

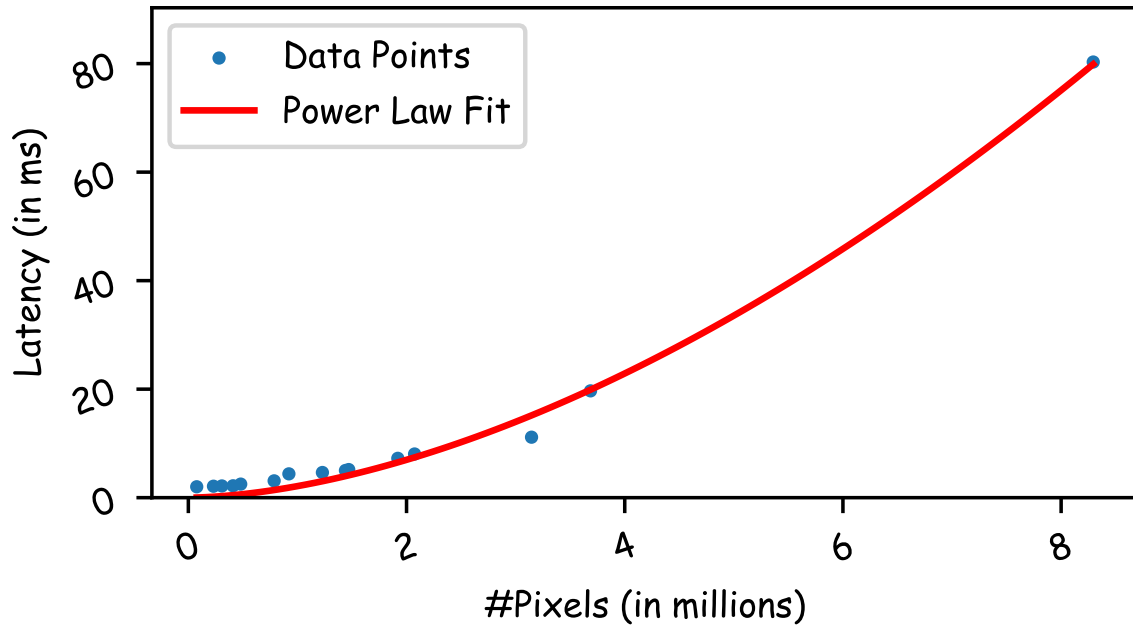


Fig. 7. Relation between the frame size and the inpainting latency

pixels) and the latency is not linear. Instead, the data indicates a power-law relationship ( $a \cdot x^b$ ), confirming that the inpainting latency is indeed a superlinear function of the input frame size.

#### 3.4.1: Insight

The inpainting task exhibits a superlinear increase in latency relative to the input frame size, making it suitable for partitioning and parallel execution.

### 3.5 Frame Segmentation

In Section 3.3, we discussed the partitioning of a frame based on how the human eye perceives distinct regions and its sensitivity to subtle variations within these regions. Building upon this foundation, in this section, we delve into the mathematical properties of these regions. We shall perform a comprehensive characterization of the rendered frames, analyzing their properties in the temporal domain [Bouwmans et al. 2018; Li et al. 2004]. This is a highly novel characterization approach for real-time graphics systems, such as Virtual Reality (VR). This novel inter-frame analysis is a basis for proposing a heuristic-based approach to distinguish and segment frames into the foreground, near-background, and far-background regions.

In the temporal domain, we analyze dynamic changes over time by capturing inter-frame variations in the pixel intensity. Mathematically, for a pixel at position  $(x, y)$  in frame  $F$ , the temporal change  $T(x, y)$  can be calculated using Equation 1.1. After computing the variation values, we apply Otsu's thresholding method [Liu and Yu 2009] to divide the frame into two primary regions: near and far. Pixels exhibiting high temporal variation are classified as part of the near region. This high variation indicates significant movement or changes in the scene.

Conversely, pixels with low variations are classified as part of the far region. These areas tend to have more stable intensity values over time. Note that these regions can be spatially disconnected.

$$T(x, y) = \frac{1}{T-1} \sum_{t=1}^{T-1} |I(x, y, t+1) - I(x, y, t)| \quad (1.1)$$

where,  $I(x, y, t)$  represents the intensity of the pixel in the frame rendered at time  $t$  and  $N$  is the total number of frames. Higher values of  $T(x, y)$  indicate greater temporal variability.

We present the segmentation results for three benchmark scenes in Figure 8. For each scene, we include the following visualizations: the original frame, computed temporal variations, a binary mask highlighting regions with high variations and a rectangle fitted around the high temporal variation regions, superimposed on the original frame. We make the following observations from the figures:

① Dynamic objects consistently appear in the regions of high temporal variations. This includes not only the moving object itself but also its immediate surroundings, which are affected by the object's movement.

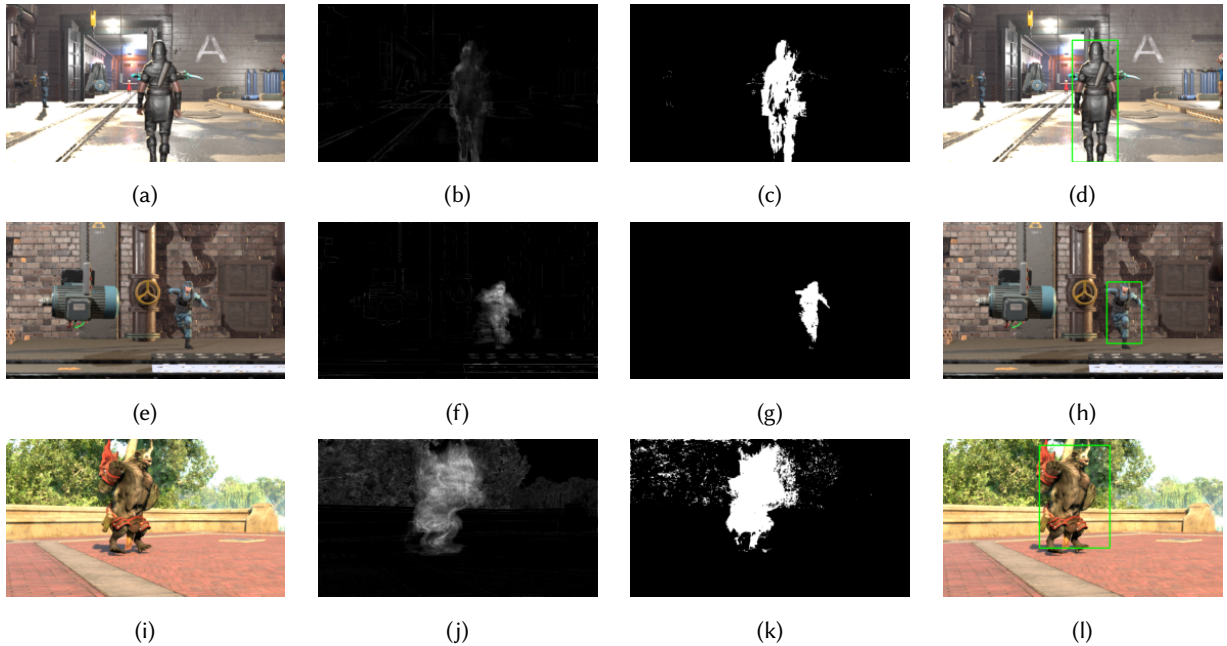


Fig. 8. (BK: (a) Original frame; (b) Temporal variations; (c) High variations mask; (d) Rectangular boundary for the near region); (BK: (e) Original frame; (f) Temporal variations; (g) High variations mask; (h) Rectangular boundary for the near region); (PR: (i) Original frame; (j) Temporal variations; (k) High variations mask; (l) Rectangular boundary for the near region).

To substantiate our findings across benchmarks, we further analyze the relationship between the dynamic objects and the high temporal variation regions. We plot the percentage of the dynamic objects' area that lies within the high variation regions along with the area of the high variation regions that is occupied by the dynamic objects (refer to Figure 9). The average coverage of the high variation regions by the dynamic objects across all benchmark scenes is approximately 96.5%. This indicates that the majority of the high variation regions are

occupied by the dynamic objects. 82.6% of the dynamic objects' area falls within the high variation regions. This high percentage demonstrates that the maximum temporal variation is in the regions where dynamic objects are present, with a small amount of exclusion.

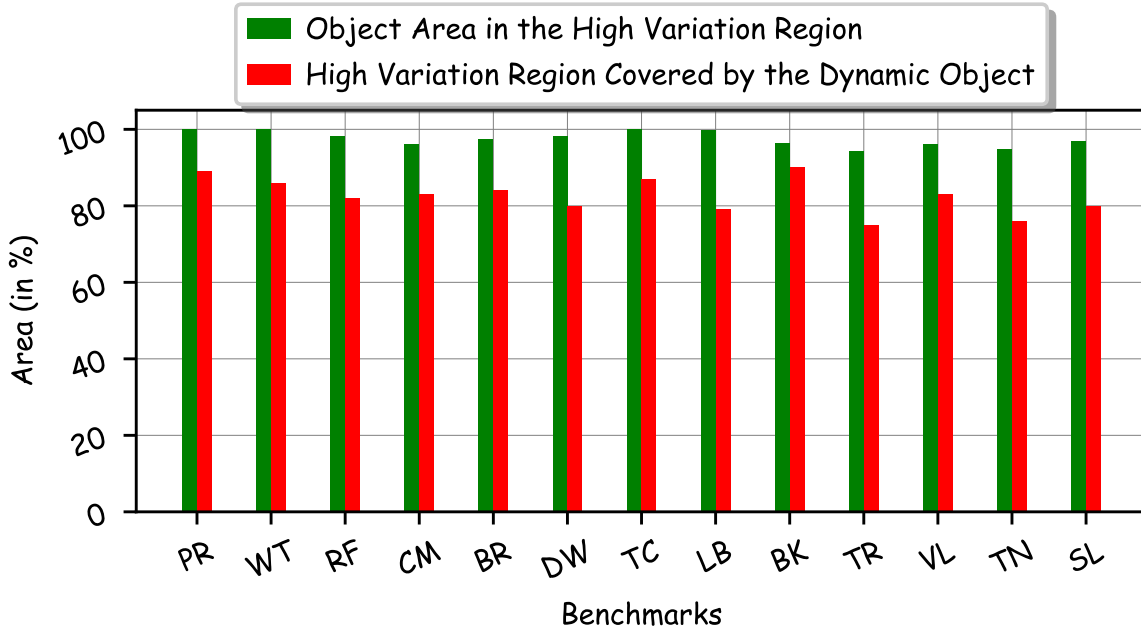


Fig. 9. Analysis of the high variation regions and coverage of dynamic objects

In order to find the rectangular borders of the foreground, near-BE and far-BE regions in real time, we have developed a heuristic-based method. This approach is necessary because it is not feasible to use future frames for analyzing variations between frames in real time. To facilitate this heuristic approach, we analyze the data to detect patterns and correlations between the dimensions of the rectangular boundaries and the average motion. For each frame, we measure the average motion in the x-direction ( $\mu_x$ ) and the y-direction ( $\mu_y$ ) and the corresponding width ( $w$ ) and height ( $h$ ) of the rectangular boundaries for the regions with high temporal variation. Then, we calculate the Pearson correlation coefficient for  $w$  and  $\mu_x$ , and for  $h$  and  $\mu_y$  (see Figure 10). The correlation coefficient helps us quantify the strength and direction of the linear relationship between these variables. We make the following observations from the results:

❶ For a given dynamic object, the width of the rectangular boundary has a strong positive correlation with the average motion in the x-direction ( $\mu_x$ ). The average Pearson's correlation coefficient is 0.78. Additionally, the height of the rectangular boundary has a strong positive correlation with the average motion in the y-direction ( $\mu_y$ ), with an average correlation coefficient of 0.79.

❷ These strong correlations provide a solid foundation for our heuristic approach for real-time frame segmentation. By leveraging the linear relationships between boundary dimensions and motion, we can estimate the rectangular boundary in real-time without needing future frame data.



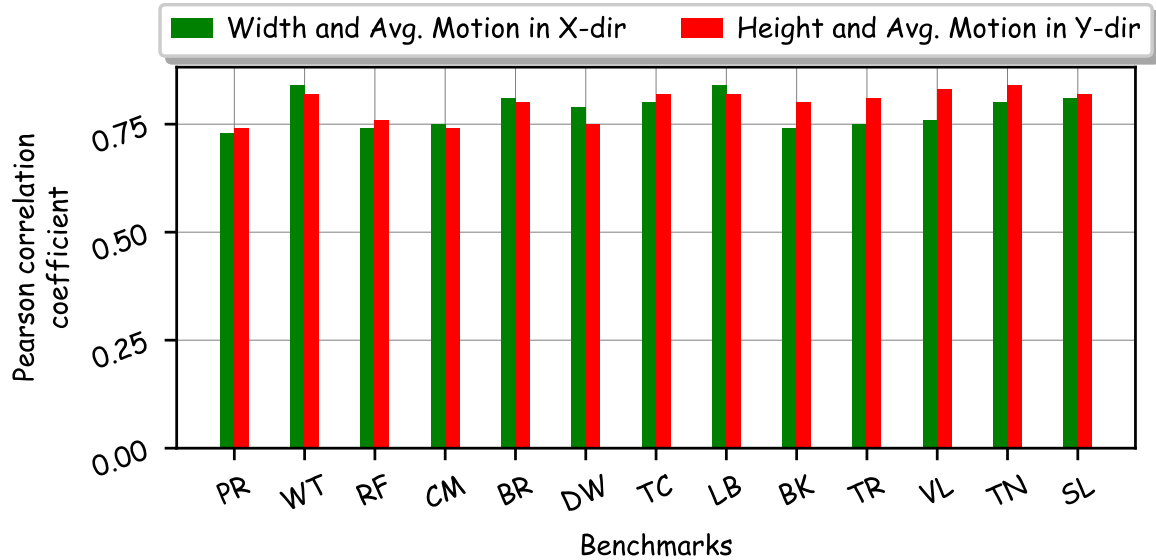


Fig. 10. Relationship between boundary dimensions and average motion

### 3.5.1: Insight

By analyzing the motion patterns of dynamic objects, we can effectively segment a frame into foreground, near-BE and far-BE regions.

## 3.6 Performance of Various Warping Methods

In Fig. 11, we present the results of various warping techniques including traditional motion vector-based warping, occlusion motion vector-based warping and G-buffer-based warping, in comparison to the ground truth. The results demonstrate that both motion vector-based warping methods exhibit some degree of ghosting, which affects the overall quality of the output. However, in the case of G-buffer-based warping, ghosting is absent but it leads to incorrect shading in the resulting frame. Ghosting is absent here because the knowledge of disoccluded objects is present in the G-Buffers and this information can be used to fill in the gaps. Therefore, our approach utilizes G-buffer-based warping as an initial prediction. This addresses the first challenge to some extent (much more needs to be done).

## 3.7 Challenges in Frame Extrapolation

Our primary objective is to predict an intermediate frame called  $F_{t+0.5}$  by utilizing the previously rendered frame,  $F_t$ . We can achieve this goal due to two primary reasons. First, there are similarities between frames in any graphics application. Second, we have some internal information from the rendering pipeline, such as motion vectors that indicate the position of the pixels in the next frame.

However, this task is not as simple as it seems, and there are two significant challenges with motion-vector-based approaches. Since we are extrapolating, we only have motion vectors in one direction, which implies that



Fig. 11. Comparison of various warping techniques

we can accurately predict regions that were present in both the frames  $F_t$  and  $F_{t+1}$ . However, for the disoccluded regions in frame  $F_{t+1}$ , the motion vectors do not provide any information, and we don't know how to fill those pixels correctly – this makes the extrapolation task extremely challenging. Furthermore, there are three categories of occlusions: self, object-to-object and object-to-background, which also means that three types of disoccluded regions exist (refer to Fig. 12). Self-occlusion occurs when an object obstructs itself in the image. Object-to-object occlusion happens when two or more objects overlap, and object-to-background occlusion occurs when an object is partially or wholly occluded by the background. These disoccluded regions remain a challenge to fill in, making the extrapolation task even more complex.

The other challenge in the extrapolation task is accurately predicting changes in *shadows*. Even minor changes in the movement of a dynamic object can result in significant changes in the shadow it casts, as illustrated in Fig. 13. This can have a significant impact on the overall realism of graphics applications, as shadows play a crucial role in conveying depth and dimensionality.

To tackle these two challenges, we divide the extrapolation task into two parts. The first part focuses on correctly extrapolating the frame except for the shadow. This involves predicting the movement and transformations of objects in the scene while ignoring changes in the shadow. The second part deals exclusively with predicting the shadow. This involves accurately predicting how the shape, size, and intensity of the shadow will change over time as the object moves and the lighting conditions in the scene change.

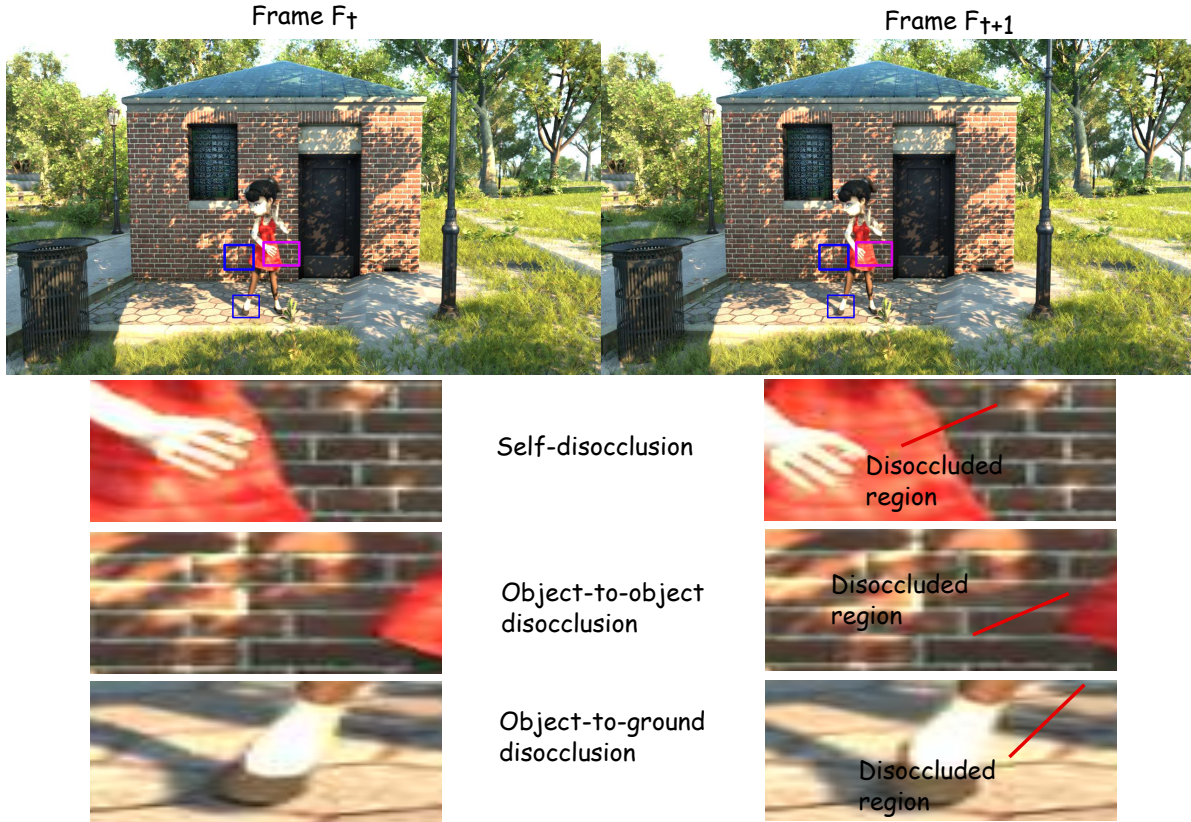


Fig. 12. Possible disoccluded regions in a frame

### 3.7.1: Insights

- ❶ The presence of disoccluded regions (□) and sudden changes in the shadows (●) pose a significant challenge for frame extrapolation.
- ❷ We propose two segmentation approaches: first, separating shadows from the rendered frame, and second, divide the rendered frame (without shadows) into three patches (foreground, near-BE and far-BE) by leveraging foreground bias and near-object effects. These segmentation techniques aim to address challenges associated with frame extrapolation.

## 4 METHODOLOGY

In this section, we establish a formal definition of the frame extrapolation problem before detailing our methodology. Our primary objective is to predict the intermediate frame  $F_{t+0.5}$  based on the preceding frame  $F_t$  and a few G-buffers. In simple terms, we aim to generate a frame that visually sits halfway between two consecutive frames while ensuring coherence with the overall sequence of frames. To achieve this, our method is organized into five separate stages as shown in Fig. 14. These five stages are as follows:

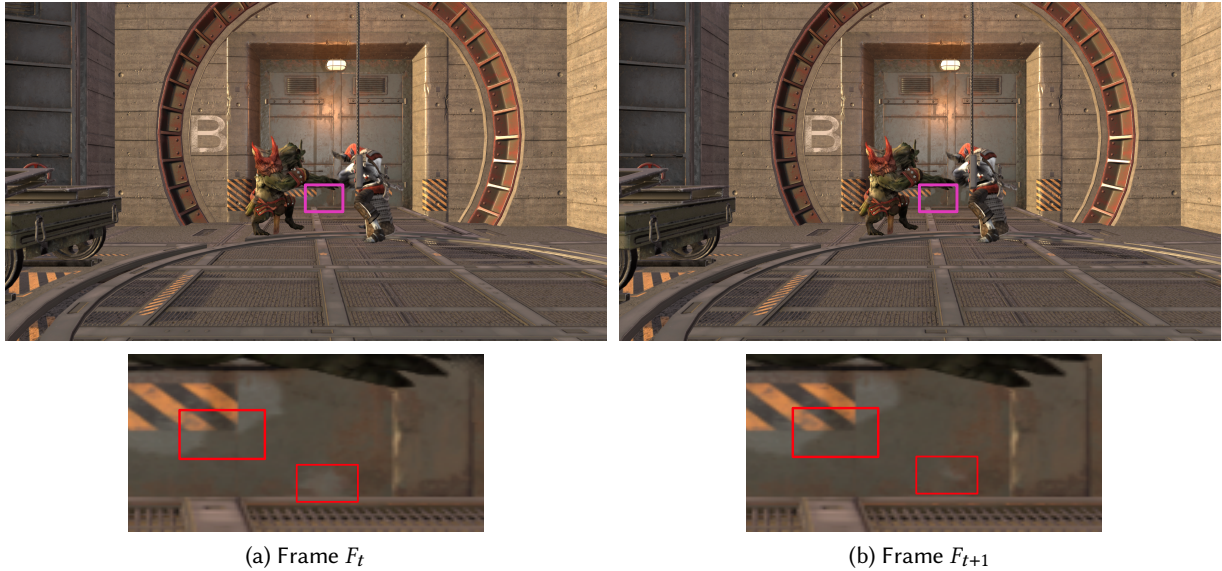


Fig. 13. Dynamic changes in the appearance of shadows between two successive frames,  $F_t$  and  $F_{t+1}$ .

- (1) **Data Extraction:** The first stage is data extraction, where we run the applications on the Unreal Engine. In this phase, we extract various G-buffers utilizing custom render passes. Subsequently, we preprocess the extracted data to ensure its compatibility with the subsequent stages. In addition to the G-buffers, we extract the shadow information from the rendering engine.
- (2) **Segmentation mask generation:** In this stage, we create three binary masks that partition the rendered frame into three distinct patches: foreground, near-background (near-BE), and far-background (far-BE). As discussed in Section 3.3, only dynamic objects in the frame are identified as the foreground, while the rest of the screen area is considered as the background. Hence, the stencil G-buffer, which serves as a mask for dynamic objects is assigned as the foreground mask (refer Fig.15). Next, to find the near-BE region, we initially define a bounding rectangle around dynamic objects and subsequently expand its dimensions by small increments determined by the motion vector. This expanded bounding rectangle is then assigned as the mask for the near-BE region, while the residual area constitutes the far-BE mask.
- (3) **Data preprocessing:** Here, we perform two critical tasks. First, we execute G-buffer-guided warping and then identify *invalid pixels* in the warped frame. Subsequently, we perform a bitwise *AND* operation between the three segmentation masks and the warped frame to create three distinct input sets for extrapolation. For shadows, we utilize the shadow mask extracted from Frame  $F_t$  to compute the motion vectors.
- (4) **Extrapolation:** As outlined in Section 1, we employ two different bespoke neural networks to extrapolate the foreground and near-BE regions. For the far-BE region, we retain the warped frame as it is. Concurrently, we extrapolate shadows using the motion vectors computed in the previous stage.
- (5) **Blending:** This stage involves merging the outputs from the three extrapolation methods along with the predicted shadow. This integrated approach ensures an accurate extrapolated frame.

In the following section, we will provide a detailed discussion of our proposed method.

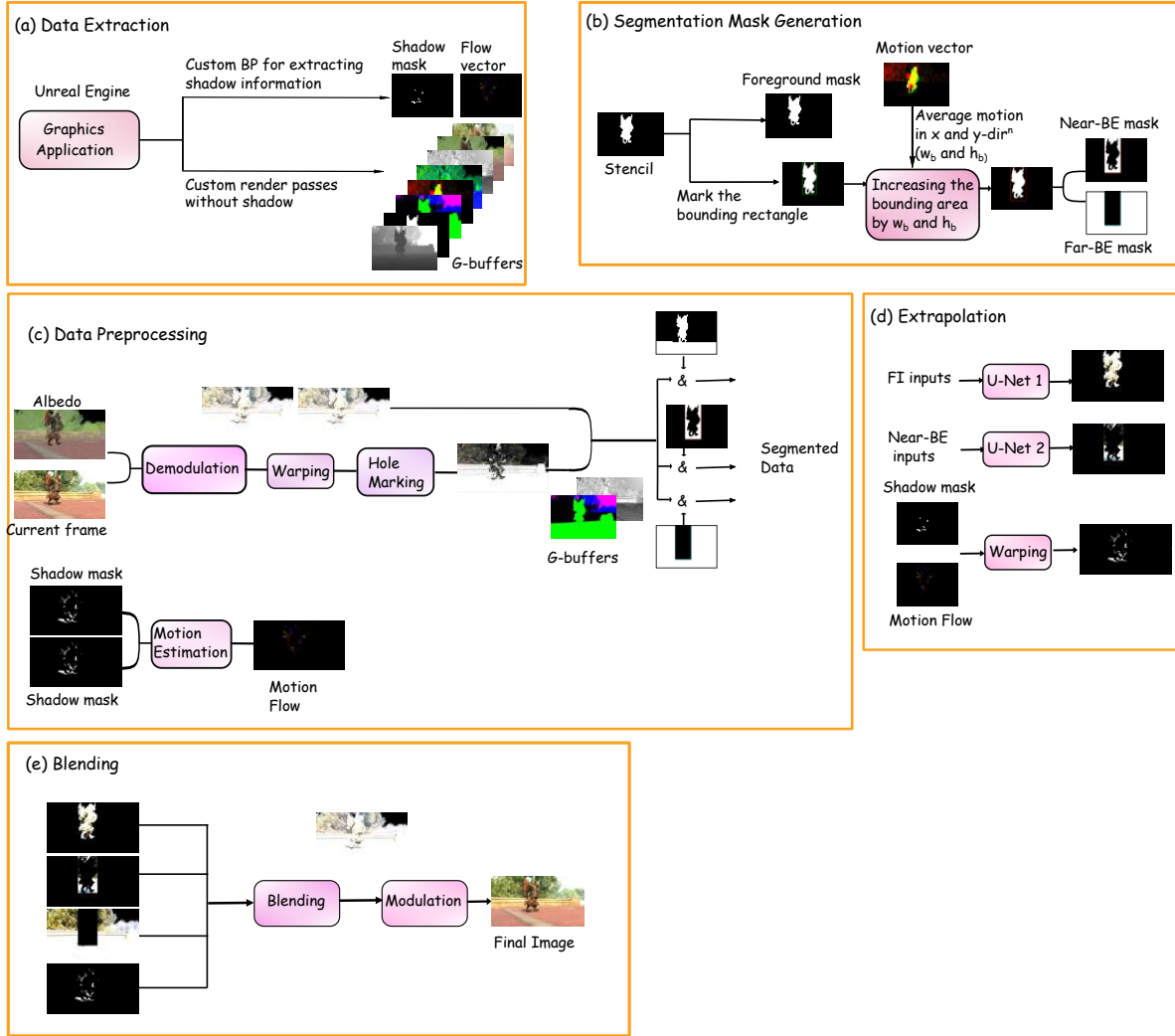


Fig. 14. Overview of our proposed approach. (a) *Data Extraction*: We extract a few G-buffers using custom render passes and obtain the shadow information using a custom blueprint (BP) class from the Unreal Engine (UE). (b) *Segmentation*: We create three binary masks to segment the frames into the foreground, near-BE, and far-BE regions. (c) *Data Preprocessing*: Using the extracted G-buffers, we warp  $F_t$ , mark invalid pixels or holes in the warped frame, and segment the warped frame into three distinct regions. For shadows, we compute the motion flow. (d) *Extrapolation*: We use two different neural networks to extrapolate the foreground and near-BE regions, while the warped frame is used for the far-BE region. For shadow extrapolation, we employ occlusion motion-vector-based warping. (e) *Blending*: Finally, we merge the three extrapolated regions and the shadows to produce the final image.

## 5 IMPLEMENTATION

### 5.1 Data Extraction

For every frame, we extract the following G-buffers from the Unreal engine: scene depth, world normal, world position, custom stencil, pretonemap, NoV (normal over view vector) and motion vector. A visualization of all these buffers is shown in Fig. 15.

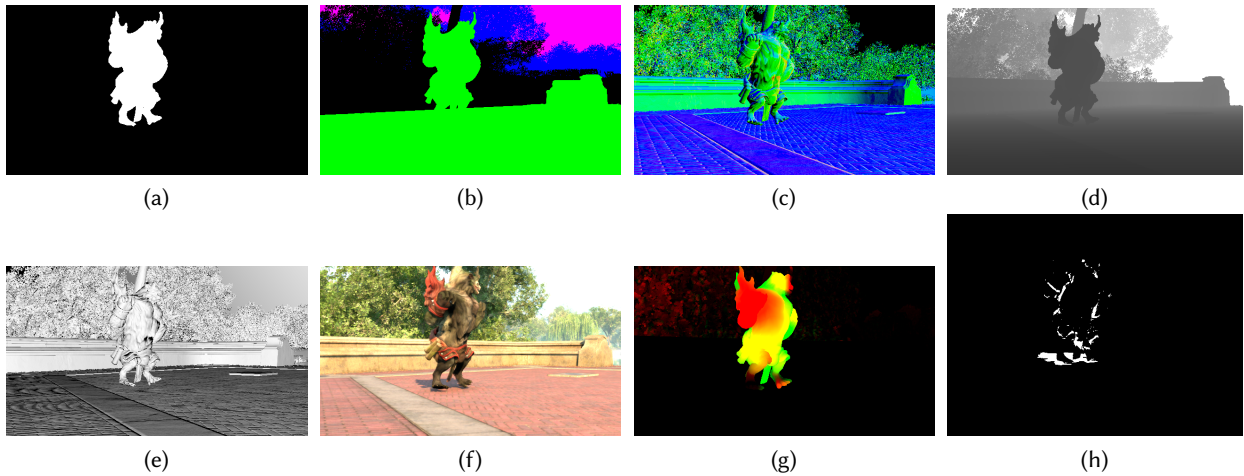


Fig. 15. (a) Stencil; (b) World Normal; (c) World Position; (d) Scene Depth; (e) NoV; (f) PretonemapHDRColor; (g) Motion Vector; (h) Shadow Mask.

### 5.2 Mask Generation for Segmentation: Create Bounding Boxes

Based on **Insights** 3.3.1 and 3.4.1, we propose to divide the frame into three patches and apply different extrapolation algorithms on each patch to generate a high-quality extrapolated frame quickly. First, we divide the frame into the foreground and background regions, followed by further dividing the background into near-BE and far-BE regions to adjust for the “near-object effect”.

Foreground detection is a complex task in video processing, but with access to G-buffers, we can efficiently separate the foreground from the background. By extracting a stencil buffer from the Unreal Engine, which stores masks for dynamic objects in the scene, we can identify and isolate these objects [Guo et al. 2021]. To further classify the background into near and far regions, we utilize the motion vector information. This classification is crucial for distinguishing regions close to the moving object from the static background, allowing us to identify areas most affected by foreground movements and potentially containing invalid pixels due to disocclusion. However, several challenges arise in separating the near and far background regions. First, determining the bounding box that encompasses the moving object is essential for demarcating the near-BE region. Additionally, given the large variety of dynamic objects that scenes may contain, it is vital to ensure that the background separation method is adaptable to different scenarios.

As mentioned in Section 3.5, we can segment the near and far-BE regions based on the temporal variation. However, the challenge lies in the real-time computation and segmentation of these regions. Hence, we propose a simpler heuristic-based approach to perform the segmentation. Based on **Insight 3.5.1**, we focus on the movement of dynamic objects to identify the near-BE region. To differentiate between the near and far background, we start

by assigning a default bounding box (based on the stencil buffer's values) to every moving object. To ensure a broader coverage area, we expand the rectangle's width and height by biases  $w_b$  and  $h_b$ , respectively, as shown in Fig. 16. These biases are not preset but are calculated based on the dynamic object's motion. Algorithm 1 outlines the complete procedure for the background classification process.

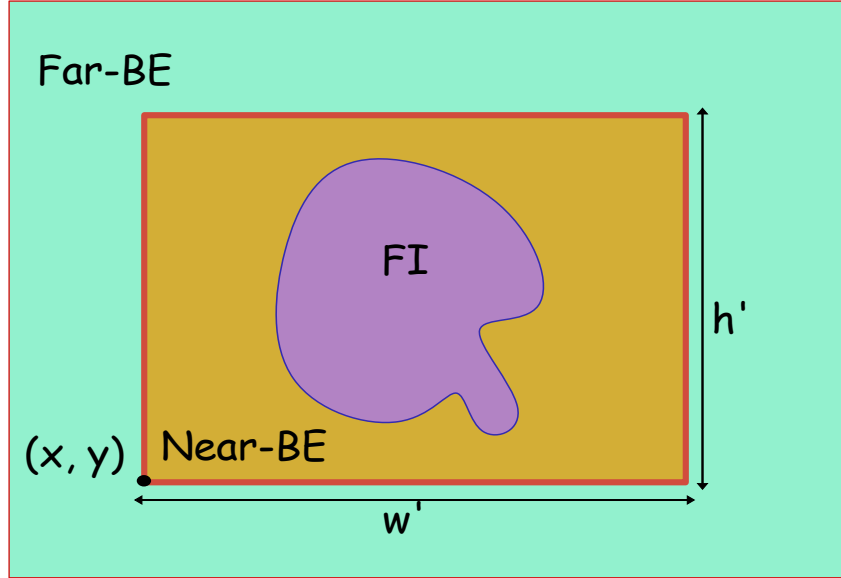


Fig. 16. Identified regions in a frame. Foreground interactions are represented by FI, while Near-BE and Far-BE refer to near and far background environments, respectively. They are separated by a rectangular bounding box of height  $h'$  and width  $w'$ .

---

**Algorithm 1** Dynamic Region Expansion for Background Classification

---

**Require:** Initial bounding rectangle surrounding the dynamic object  $\text{Rect} = (x, y, w, h)$ , motion vectors  $\vec{v}_x$  and  $\vec{v}_y$ , scaling factors  $k_x$  and  $k_y$

**Ensure:** Expanded bounding rectangle  $\text{Rect}' = (x, y, w', h')$

- 1: Compute average motion (horizontal and vertical):

$$\bar{v}_x = \frac{1}{N} \sum_{i=1}^N \vec{v}_x(i), \quad \bar{v}_y = \frac{1}{N} \sum_{i=1}^N \vec{v}_y(i)$$

- 2: Determine expansion biases:

$$w_b = k_x \cdot \bar{v}_x, \quad h_b = k_y \cdot \bar{v}_y$$

- 3: Expand the bounding rectangle:

$$w' = w + w_b, \quad h' = h + h_b$$

- 4: Output the expanded rectangle:  $\text{Rect}' = (x, y, w', h')$
-

### 5.3 Data Preprocessing

We have already discussed the process of extracting data from the Unreal Engine and creating binary masks to segment the frame into foreground, near-BE, and far-BE regions, respectively. As we plan to use different techniques for extrapolation in these three regions, we require three sets of input data. Therefore, it is necessary to preprocess the data obtained from Unreal to ensure that we have the required data in the required format.

As we have discussed earlier, to get a quick initial estimate of the final frame, we *warp* frame  $F_t$ . Prior to doing this, we need to demodulate (remove many graphics effects) the frame: previous works have shown that inpainting networks produce better results with demodulation [He et al. 2024; Wu et al. 2023a]. The demodulation formula is shown in Equation 2. As mentioned in Section 2, we opt for the G-buffer guided warping method because of its minimal ghosting effects. Subsequently, we detect invalid pixels within the warped frame by utilizing G-buffers (as described in ExtraNet [Guo et al. 2021]). Upon completion of this step, we partition the warped frame into three distinct regions utilizing the segmentation masks (Section 5.2) to generate inputs for the next stage.

$$F' = F / (\text{Albedo} + \text{Specular} * 0.08 * (1 - \text{Metallic})) \quad (2)$$

$F$  is the rendered image and  $F'$  is the image generated after demodulation.

### 5.4 Extrapolation

**5.4.1 Network Architecture.** We propose two bespoke neural networks for the foreground and near-BE region, respectively. For the far-BE region, we directly use the warped frame. The architectures of these two networks are shown in Fig. 17 and Fig. 18, respectively. Our networks are roughly similar to U-Net [Ronneberger et al. 2015] but have important differences. U-Net has an encoder-decoder architecture. Instead of using simple convolution, we have used light-weight gated convolution proposed by Yi et al. [Yi et al. 2020] in our network which is formulated as:

$$\begin{aligned} G(\text{gating}) &= \text{Conv}(W_g, I) \\ F(\text{features}) &= \text{Conv}(W_f, I) \\ O &= \sigma(G) \odot F \end{aligned} \quad (3)$$

$W_g$  and  $W_f$  denote two distinct learnable filters.  $\odot$  denotes Hadamard (element-wise) multiplication, and  $\sigma$  represents the sigmoid activation function. The latter ensures that the output gating values are in the range  $[0, 1]$ . This approach helps in treating different pixels differently in the network since there are invalid pixels in the warped frame. Our gating mechanism diminishes the influence of invalid pixels. In our neural networks, we utilize a comprehensive set of inputs: the warped frame, a hole mask indicating invalid pixels, and two G-Buffers (*Roughness* and *Metallic*). Unlike previous works, we also provide as input the LBP (local binary pattern) feature map of the warped frame. By incorporating the LBP feature map, we leverage its robust feature extraction capabilities and its resilience to uneven illumination. This addresses the challenge of extracting detailed features from images with inconsistent lighting, significantly boosting the generalizability and effectiveness of our method.

**5.4.2 Loss Functions.** The *loss function* used for training the networks has broadly two components. The first component penalizes the pixel-wise error between the ground truth  $F$  and the predicted frame  $F'$ . The second component is the perceptual loss, which was not considered in previous works [Guo et al. 2021; He et al. 2024]. The *perceptual loss* plays a crucial role in enhancing the performance of neural networks, particularly in tasks related to image inpainting [Ran et al. 2023] because it focuses on capturing high-level perceptual features, mimicking human visual perception.



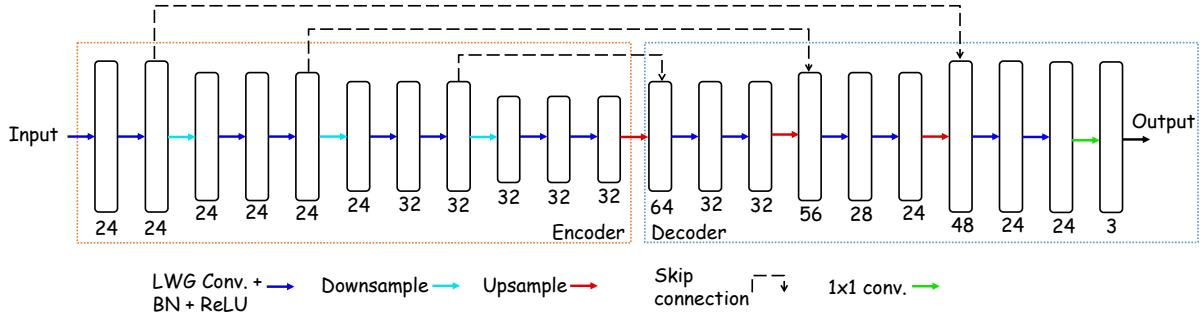


Fig. 17. The neural network architecture for extrapolating the foreground region.

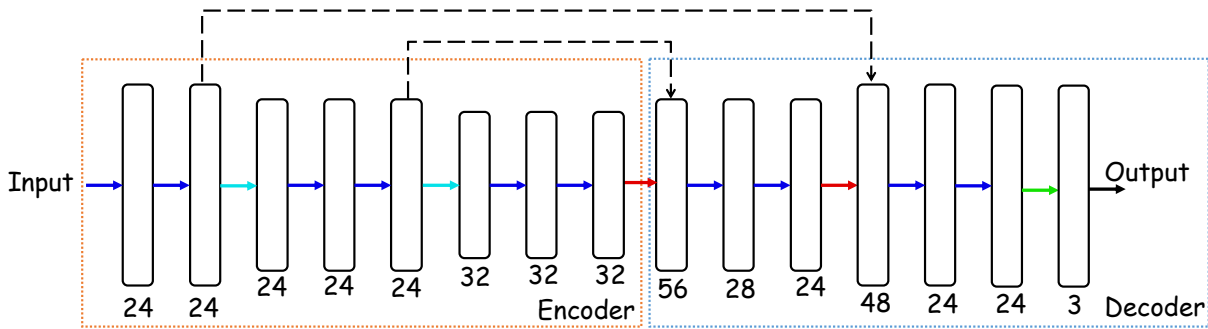


Fig. 18. The neural network architecture for extrapolating the near-BE region.

$$\mathcal{L} = \mathcal{L}_{pixel} + \mathcal{L}_{perceptual} \quad (4)$$

- **Pixel-wise Errors:** To calculate the error on a pixel-by-pixel basis, we use the  $\mathcal{L}_1$  loss, which can be computed using the formula in Equation 5. We employ the  $\mathcal{L}_1$  loss in three different forms. First, we calculate the total  $\mathcal{L}_1$  loss between the entire ground truth frame and the predicted frame. Second, we calculate the error between the pixels that were marked as holes or invalid pixels during the data preparation stage. Finally, we compute the error between the valid pixels of both frames. The total loss is the weighted average of these three losses (refer to Equation 6).

$$\mathcal{L}_{\mathcal{L}_1} = \|X - Y\|_1$$

$$\mathcal{L}_{\mathcal{L}_1} = \sum_{i=1}^H \sum_{j=1}^W |X(i, j) - Y(i, j)| \quad (5)$$

$$\mathcal{L}_{\mathcal{L}_1} = \|F - F'\|_1$$

$$\mathcal{L}_{hole} = \|(F - F') \cdot (1 - m)\|_1$$

$$\mathcal{L}_{valid} = \|(F - F') \cdot m\|_1$$

$$\mathcal{L}_{pixel} = \lambda_{\mathcal{L}_1} \cdot \mathcal{L}_{\mathcal{L}_1} + \lambda_{hole} \cdot \mathcal{L}_{hole} + \lambda_{valid} \cdot \mathcal{L}_{valid} \quad (6)$$

Table 7. Statistics of the training and testing dataset

Scenes	Training Sequences	Training Frames	Testing Sequences	Testing Frames
PR	5	5000	3	3000
WT	5	5000	3	3000
RF	5	5000	3	3000
CM	5	7000	3	3000
BR	5	5000	3	3000
DW	5	4000	3	3000
TC	5	4000	3	3000
TN	5	5000	3	3000
BK	0	0	3	3000
LB	0	0	3	3000
TR	0	0	3	3000
VL	0	0	3	3000
SL	0	0	3	3000

$m$  is a binary mask used for identifying the invalid pixels.  $\lambda_{\mathcal{L}_1}$ ,  $\lambda_{hole}$ , and  $\lambda_{valid}$  are the weights assigned to each component loss function (balance out their effects). In our current implementation,  $\lambda_{\mathcal{L}_1}$  is set to 1 and the rest of the two values are set to 0.5 each.

- **Perceptual Losses:** We adopt the perceptual loss [Johnson et al. 2016] to guide the neural network to generate an image that is more in line with human perception (refer to Equation 7).

$$\mathcal{L}_{VGG} = \mathbb{E} \left[ \sum_i \|\Phi_i(F) - \Phi_i(F')\|_1 \right] \quad (7)$$

$\Phi_i$  is the activation map of the  $i^{th}$  layer of the VGG-16 [Liu and Deng 2015] network pre-trained on ImageNet. Furthermore, we use a similar loss function called *style loss* to maintain a degree of similarity between the predicted and the original image (refer to Equation 8). The joint perceptual loss is shown in Equation 9. The key idea is that we are preventing *hallucination*, where the output of the model can be very different from the original image. The main aim is to fix the base image created by warping and not make unconstrained errors.

$$\mathcal{L}_{style} = \mathbb{E} \left[ \sum_i \|G_j^{\Phi_i}(F) - G_j^{\Phi_i}(F')\|_1 \right] \quad (8)$$

$G_j^{\Phi}$  is the Gram matrix of the VGG features extracted for the perceptual loss.

$$\mathcal{L}_{perceptual} = \lambda_{VGG} \cdot \mathcal{L}_{VGG} + \lambda_{style} \cdot \mathcal{L}_{style} \quad (9)$$

$\lambda_{VGG}$  and  $\lambda_{style}$  are the weights assigned to each loss to balance their effects. In our current implementation,  $\lambda_{VGG}$  is set to 0.1 and  $\lambda_{style}$  is set to 0.01.

**5.4.3 Training and Testing.** In our work, we utilize 13 benchmark scenes as discussed in Section 5.1. These scenes are divided into two groups: nine for training and four for testing. For each scene, we have created five animation sequences for training and three sequences for testing. The number of frames in each sequence varies. The total number of frames for training and testing for each scene are specified in Table 7. We implemented both the neural networks using the PyTorch framework [Paszke et al. 2019]. To divide the data for training and validation in an 80:20 ratio, we utilized PyTorch's inbuilt *random\_split* function.

**5.4.4 Training Details.** Both our neural networks are implemented and trained using the PyTorch framework [Paszke et al. 2019]. We utilize the Adam optimizer for optimization with batch sizes set to 16 and epoch sizes to 100. The network initialization is as per the default settings in PyTorch.

## 5.5 Blending

In the final stage of the process, we bring together all three extrapolated regions: FI, near-BE, and far-BE. As previously mentioned, we first demodulate the frame before carrying out the warping process and feed it to the neural networks. To blend the three extrapolated regions, we use a mask-based image blending algorithm [Xiong and Pulli 2009], which is a type of weighted blending. The final blending equation is shown in Equation 10. Consequently, we need to modulate the final merged frame back using Equation 11. Before modulation, we also need to blend the warped shadow, which will be explained in Section 5.6.

$$F = M_1 * F_1 + M_2 * F_2 + M_3 * F_3 \quad (10)$$

$M_1$ ,  $M_2$  and  $M_3$  are the segmentation masks (binary masks) for the foreground, near-BE and far-BE regions, respectively.  $F_1$ ,  $F_2$  and  $F_3$  are the extrapolated versions of those regions.

$$F' = F * (Albedo + Specular * 0.08 * (1 - Metallic)) \quad (11)$$

## 5.6 Extrapolation of Shadows

In the first stage, the data extraction stage, we extract the shadow mask for all dynamic objects using a custom blueprint class in the Unreal Engine. In the preprocessing stage, we process the shadow mask obtained from Unreal Engine. As previously discussed, we perform shadow warping to compute the extrapolated shadow. We begin by estimating the motion flow between shadows using Farneback’s algorithm [Farneback 2003]. In the extrapolation stage, we use the computed motion flow to warp the shadow. As discussed in Section 3.6, traditional warping produces a ghosting effect in the warped frame. Therefore, we use occlusion motion vector-based warping. It is important to note that this process runs in parallel with the inpainting networks. Finally, in the blending stage, we blend the warped shadow with the blended extrapolated regions (the output of Equation 10) using an additive blending approach, which simply adds the two images on a pixel-by-pixel basis. In the end, the resulting image is modulated using Equation 11.

# 6 RESULTS AND ANALYSIS

To demonstrate the performance of the proposed method, *PatchEX*, we compare it against various state-of-the-art works in both the domains of frame interpolation and extrapolation. Since all these works are ML-based solutions, we fine-tune their proposed neural networks for our dataset before comparing the performance. After that, we perform an ablation study to evaluate the contribution of various individual components to the overall performance. Next, we measure the runtime latency for each component of *PatchEX*. For all these experiments, we use the same system configuration (refer to Table 4).

## 6.1 Performance Metrics

To measure the performance of *PatchEX*, we use three widely used performance metrics: PSNR (Peak Signal-to-Noise Ratio), SSIM (Structural Similarity Index), and LPIPS (Learned Perceptual Image Patch Similarity) [Belhe et al. 2023; Paliwal et al. 2023].

PSNR, as its name suggests, is a ratio between the maximum possible power for an image and the power of the noise signal present in the image (refer to Equation 12). This means that higher PSNR values signify higher quality. However, PSNR measures the quality of images globally while ignoring local distortions. Hence, we cannot solely depend upon PSNR to assess the performance.

Next, we use SSIM, which computes the structural similarity between two images by capturing the local patterns and textures. It also captures the brightness and contrast information. SSIM is computed using Equation 13. SSIM values range from -1 to 1, where 1 indicates perfect similarity.

Unlike PSNR and SSIM, which simply perform pixel-wise comparison, the next performance metric we use, LPIPS, computes the perceptual similarity using an ML model. It uses a deep neural network that extracts features from the images and then compares the extracted features. A comparison in the feature domain aligns better with human perception. LPIPS values range from 0 to 1, and higher LPIPS values indicate that the images are more dissimilar.

$$PSNR = 10 \times \log_{10} (MAX^2 / MSE) \quad (12)$$

where,

- MAX is the maximum possible pixel value of the image (typically 255 for 8-bit images).
- MSE is the mean squared error between the original and reconstructed images.

$$SSIM(x, y) = \frac{(2\mu_x\mu_y + c_1)(2\sigma_{xy} + c_2)}{(\mu_x^2 + \mu_y^2 + c_1)(\sigma_x^2 + \sigma_y^2 + c_2)} \quad (13)$$

where,

- $x$  and  $y$  are input images.
- $\mu_x$  and  $\mu_y$  are the arithmetic means of  $x$  and  $y$ , respectively.
- $\sigma_x^2$  and  $\sigma_y^2$  are the variances of  $x$  and  $y$ , respectively.
- $\sigma_{xy}$  is the covariance of  $x$  and  $y$ .
- $c_1$  and  $c_2$  are small constants (to avoid division by zero).

## 6.2 Performance Comparison with the Frame Extrapolation Methods

In this section, we compare the performance of ExtraNet [Guo et al. 2021] and ExtraSS [Wu et al. 2023a] with our proposed method, *PatchEX*, both qualitatively and quantitatively. As mentioned in Section 2.2.2, ExtraNet and ExtraSS are the two state-of-the-art methods that perform frame extrapolation in real-time. However, ExtraSS does not solely extrapolate in the temporal domain; it also extrapolates in the spatial domain. Since we are dealing with temporal supersampling, we only consider its temporal component for the purpose of comparison.

**6.2.1 Qualitative Comparisons.** In this section, we compare the quality of the frame generated using various extrapolation methods. In Fig. 19, we show the extrapolated frames for five distinct benchmark scenes. Out of these five scenes, only one scene, *DW*, is captured with moving camera settings. For the rest of the scenes, the camera is static, only the objects are moving.

As explained in the insights in Section 3.7.1, the challenges for extrapolation algorithms are to properly fill the disoccluded regions created by the movements in the scene and to extrapolate the shadows accurately. Both ExtraNet and ExtraSS fail to address these challenges effectively in many scenarios. For example, ExtraNet does not generate accurate shadows for complex movements such as the kick in the *FR* scene. It also performs poorly in capturing complex structures such as tree leaves and facial features in scenes like *BK*, *FR*, and *WT*. On the other hand, ExtraSS leverages G-buffer-guided warping and performs better than ExtraNet in most cases. However, it is unable to correctly extrapolate facial features during intricate motions like those in a hip-hop dance. In the *DW* scene, where the camera is moving, and parts of the scene move out of the screen, ExtraSS handles the out-of-screen areas well, whereas ExtraNet does not. *PatchEX* handles all of these complex cases pretty well. To summarize, *PatchEX* excels by not only preserving sharp features and intricate geometries but also generating plausible shadows that closely match the ground truth. We have uploaded a video of our results, which can be accessed using this link [Authors 2024].

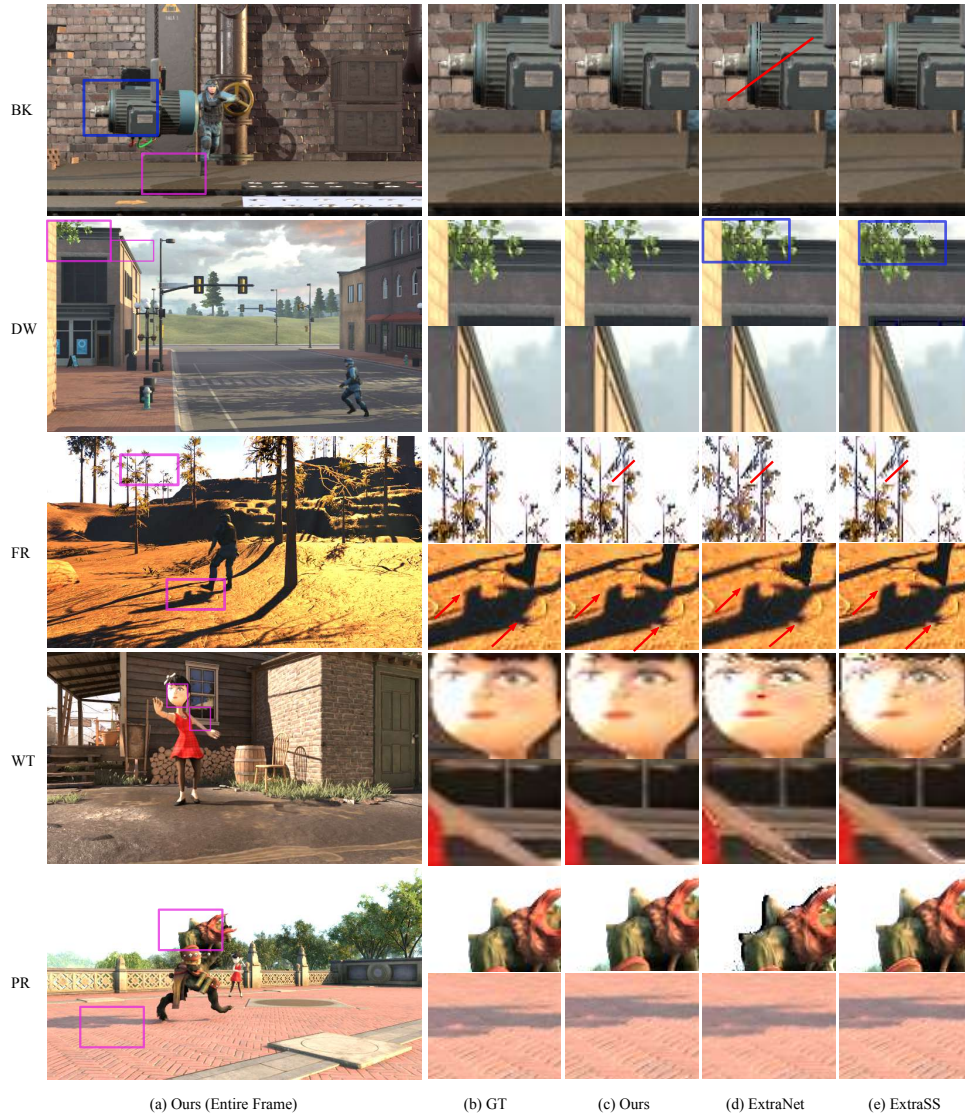


Fig. 19. Visual comparisons against two frame extrapolation methods: ExtraNet [Guo et al. 2021] and ExtraSS [Wu et al. 2023a]

**6.2.2 Quantitative Comparisons.** In this section, we perform a quantitative comparison among *PatchEX*, ExtraNet, and ExtraSS using three performance metrics: PSNR, SSIM, and LPIPS. We show the final results in Table 8 and make the following observations:

❶ Our method performs better than ExtraNet and ExtraSS across all benchmarks for all the performance metrics.

❷ There is 65.29%, 32.76%, and 92.66% increase in PSNR, SSIM, and LPIPS in *PatchEX*, respectively, as compared to ExtraNet.

Table 8. Quantitative comparison of various extrapolation methods against *PatchEX* in terms of PSNR (dB), SSIM, and LPIPS.

Scenes	PSNR (dB) ↑			SSIM ↑			LPIPS ↓		
	ExtraNet	ExtraSS	<i>PatchEX</i>	ExtraNet	ExtraSS	<i>PatchEX</i>	ExtraNet	ExtraSS	<i>PatchEX</i>
PR	28.78	21.87	<b>36.49</b>	0.909	0.948	<b>0.988</b>	0.111	0.118	<b>0.006</b>
BK	20.21	24.26	<b>37.38</b>	0.880	0.906	<b>0.991</b>	0.190	0.185	<b>0.007</b>
WT	24.01	23.75	<b>40.38</b>	0.848	0.796	<b>0.981</b>	0.213	0.109	<b>0.008</b>
RF	17.51	21.55	<b>36.55</b>	0.733	0.785	<b>0.995</b>	0.342	0.261	<b>0.005</b>
CM	33.24	22.97	<b>30.72</b>	0.867	0.502	<b>0.765</b>	0.226	0.261	<b>0.117</b>
BR	24.69	26.55	<b>34.78</b>	0.583	0.614	<b>0.987</b>	0.465	0.384	<b>0.009</b>
DW	19.63	25.03	<b>36.55</b>	0.791	0.876	<b>0.984</b>	0.376	0.169	<b>0.024</b>
TC	22.36	23.78	<b>31.63</b>	0.629	0.705	<b>0.980</b>	0.362	0.398	<b>0.022</b>
LB	24.49	27.54	<b>38.59</b>	0.846	0.901	<b>0.989</b>	0.414	0.091	<b>0.011</b>
TR	17.40	27.86	<b>34.92</b>	0.637	0.677	<b>0.985</b>	0.445	0.295	<b>0.021</b>
VL	22.19	21.00	<b>39.23</b>	0.817	0.818	<b>0.995</b>	0.314	0.178	<b>0.023</b>
TN	17.39	26.91	<b>37.35</b>	0.754	0.815	<b>0.995</b>	0.305	0.205	<b>0.009</b>
SL	16.47	28.12	<b>42.19</b>	0.467	0.510	<b>0.998</b>	0.496	0.549	<b>0.054</b>

③ Compared to ExtraSS, our method achieves an improvement of 48.46%, 31.53%, and 90.24% in PSNR, SSIM, and LPIPS, respectively.

### 6.3 Performance Comparison with Frame Interpolation Methods

In this section, we compare the performance of *PatchEX* with two state-of-the-art interpolation-based methods. The interpolation-based methods are Softmax Splatting [Niklaus and Liu 2020] and EMA-VFI [Zhang et al. 2023]. All these methods are DNN-based techniques. Softmax splatting uses forward warping; it uses forward and backward motion flow (reprojection). However, in this approach, multiple pixels may map to the same target location in frame  $F_t$ . Softmax splatting uses a modified softmax layer, which takes the frame’s depth data to resolve this ambiguity. EMA-VFI uses a transformer network to perform frame interpolation.

**6.3.1 Qualitative Comparisons.** In this section, we conduct a qualitative comparison. It is important to note that while all interpolation methods necessitate pre-rendered future frames, our extrapolation-based method exclusively relies on historical frames that have already been rendered. Consequently, interpolation methods generally exhibit superior performance compared to our method; however, there are instances where they exhibit shortcomings. To illustrate such cases, we present frames from three distinct scenes in Fig. 20, emphasizing the visual quality and effectiveness of each approach.

In the *PR* scene, both interpolation-based techniques produce shadows that closely resemble the ground truth. However, in the *BK* scene, the sharp definition of the shadow structure is compromised for both these methods. This can be attributed to the higher glossiness factor present in the *BK* scene as compared to others. Notably, our method excels in this scenario due to its utilization of G-Buffer information, which incorporates glossiness data. Another notable artifact in interpolation methods is the potential for blurriness during complex movements, as observed in the *WT* scene. We have uploaded a video of our results, which can be accessed using this link [Authors 2024].

**6.3.2 Quantitative Comparisons.** In addition to the qualitative analysis, we also perform a quantitative comparison of the frame interpolation methods. Table 9 presents the quantitative evaluation in terms of the PSNR, SSIM, and LPIPS metrics. From these results, we make the following observations:



Fig. 20. Visual comparisons against two frame interpolation methods: EMA-VFI [Zhang et al. 2023] and Softmax-splatting (SS) [Niklaus and Liu 2020]

❶ Quantitatively, interpolation-based methods perform better than *PatchEX*; however, the difference is not significant. On average, our method shows only a 12.35% decrease in PSNR compared to EMA-VFI and an 11.06% decrease compared to Softmax-splatting.

❷ For SSIM, there are several instances where our method outperforms the others. This is because interpolation can cause blurriness, which significantly impacts structural details, leading to a lower SSIM value.

❸ Even for LPIPS, our method performs reasonably well, achieving an average value of 0.024 (lower the better).

#### 6.4 Performance Analysis for High-Resolution Frames

In this area, the standard practice is to perform temporal supersampling at a resolution of 360p and then use spatial supersampling to increase the resolution. All the prior work in this area [ ] have done the same. Akin to our paper, they assume that the spatial supersampling technique is orthogonal.

Nevertheless, for gaining valuable insights into the efficiency of our algorithm let us evaluate its effectiveness when we *directly work* with frames at a full-HD resolution (1080p). This is a *though experiment*. We maintain the same experimental setup and use the same evaluation metrics.

Figure 21 shows that the extrapolated frames in this setting closely match the ground truth. Table 10 presents the average PSNR, SSIM, and LPIPS values across benchmarks for various frame resolutions. In the interest of saving space, we are not showing all the results. However, a comparison with *ExtraSS* that has a built-in spatial supersampler must be done. Representative results are shown in Table 10.

Table 9. Quantitative comparison of various interpolation methods against *PatchEX* in terms of PSNR (dB), SSIM, and LPIPS.

Scenes	PSNR (dB) ↑			SSIM ↑			LPIPS ↓		
	EMA-VFI	SS	<i>PatchEX</i>	EMA-VFI	SS	<i>PatchEX</i>	EMA-VFI	SS	<i>PatchEX</i>
PR	<b>40.08</b>	39.50	36.49	<b>0.994</b>	<b>0.994</b>	0.988	<b>0.002</b>	<b>0.002</b>	0.006
BK	<b>43.42</b>	42.82	37.38	<b>0.996</b>	<b>0.996</b>	0.991	0.002	<b>0.001</b>	0.007
WT	<b>44.87</b>	44.31	40.38	<b>0.996</b>	<b>0.996</b>	0.981	0.004	<b>0.001</b>	0.008
RF	<b>38.49</b>	37.83	36.55	0.992	0.990	<b>0.995</b>	0.003	<b>0.001</b>	0.005
CM	<b>43.96</b>	43.62	30.72	<b>0.985</b>	0.982	0.765	0.006	<b>0.003</b>	0.017
BR	<b>36.48</b>	36.27	34.78	<b>0.988</b>	<b>0.988</b>	0.987	0.007	<b>0.005</b>	0.009
DW	<b>44.04</b>	43.37	36.55	<b>0.995</b>	<b>0.995</b>	0.984	0.001	<b>0.001</b>	0.024
TC	<b>36.27</b>	35.79	31.63	<b>0.991</b>	<b>0.991</b>	0.980	0.005	<b>0.003</b>	0.022
LB	<b>45.77</b>	44.91	38.59	0.996	<b>0.997</b>	0.989	<b>0.001</b>	<b>0.001</b>	0.011
TR	<b>37.07</b>	36.69	34.92	<b>0.991</b>	0.990	0.985	<b>0.004</b>	<b>0.004</b>	0.021
VL	<b>44.24</b>	43.26	39.23	<b>0.997</b>	<b>0.997</b>	0.995	<b>0.001</b>	<b>0.001</b>	0.023
TN	<b>41.48</b>	40.92	37.35	<b>0.996</b>	<b>0.996</b>	0.995	0.002	<b>0.001</b>	0.009
SL	<b>47.64</b>	46.66	42.19	0.994	0.996	<b>0.998</b>	<b>0.001</b>	<b>0.001</b>	0.054

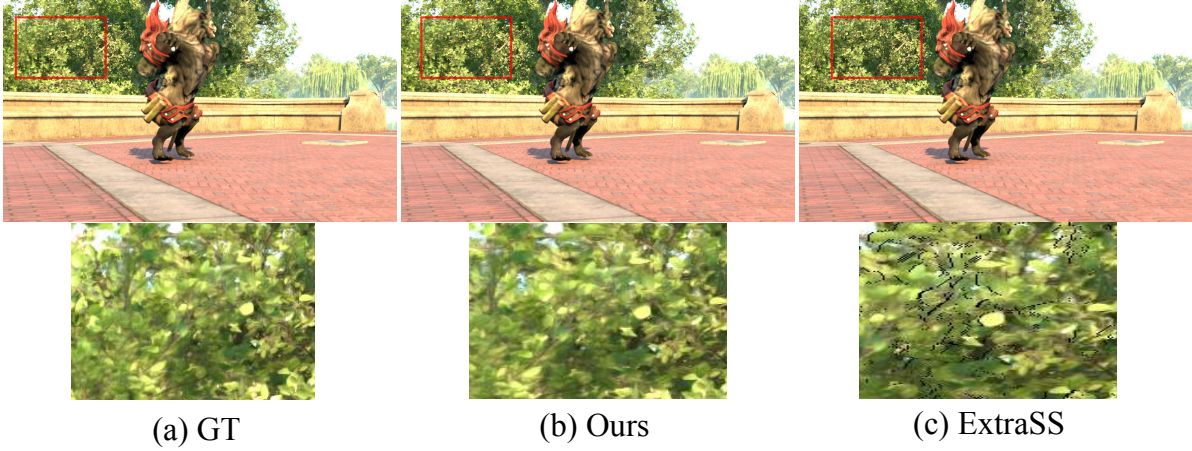


Fig. 21. Performance on high-resolution frames

## 6.5 Ablation Study

To thoroughly understand the impact of different components in our method, we conducted an ablation study focusing on three key elements: perceptual loss, foveated segmentation and the separate handling of shadows and inpainting. This analysis helps to isolate the contribution of each component in the overall performance of our frame extrapolation technique. We evaluate three distinct variants of *PatchEX*: one where shadow and inpainting tasks are not partitioned, another without foveated segmentation and a third without perceptual loss. The quantitative comparison of these variants along with the original method is shown in Table 11.

We make the following observations from the results:

- ❶ These results highlight the significant impact of foveated segmentation on improving image quality. Without foveated segmentation, the average PSNR decreases by almost 2.5 dB.
- ❷ Similarly, we see the impact of shadow and image partitioning; there is an improvement of 1.9 dB in PSNR.



Table 10. Performance of *PatchEX* in terms of average PSNR (dB), SSIM, and LPIPS at various resolution levels.

Scene res.	<i>PatchEX</i>			ExtraSS		
	PSNR↑	SSIM↑	LPIPS↓	PSNR↑	SSIM↑	LPIPS↓
360p	36.67	0.971	0.024	24.70	0.758	0.246
480p	35.90	0.967	0.035	22.98	0.769	0.258
720p	36.23	0.963	0.019	21.88	0.747	0.247
1080p	36.25	0.969	0.026	20.77	0.718	0.218

Table 11. Quantitative comparison of various variants of *PatchEX* in terms of PSNR (dB), SSIM, and LPIPS. *w/o FS* refers to without foveated segmentation. *w/o SP* refers to the case where shadow and the inpainting tasks are not handled separately. *w/o  $\mathcal{L}_p$*  refers to the case where perceptual loss is not taken into account.

Scenes	PSNR (dB) ↑				SSIM ↑			
	w/o FS	w/o SP	w/o $\mathcal{L}_p$	<i>PatchEX</i>	w/o SP	w/o FS	w/o $\mathcal{L}_p$	<i>PatchEX</i>
PR	34.32	35.40	35.50	36.49	0.985	0.985	0.985	0.988
BK	33.91	36.64	36.61	37.38	0.990	0.991	0.992	0.991
WT	38.70	31.55	39.71	40.38	0.994	0.995	0.984	0.981
RF	34.43	35.44	35.43	36.55	0.991	0.993	0.993	0.995
CM	30.59	30.52	30.54	30.72	0.761	0.759	0.760	0.765
BR	31.42	33.10	32.44	34.78	0.979	0.981	0.979	0.987
DW	35.04	35.83	35.82	36.55	0.981	0.982	0.982	0.984
TC	28.54	30.28	29.91	31.63	0.974	0.979	0.977	0.980
LB	34.26	36.75	37.01	38.59	0.985	0.988	0.988	0.989
TR	31.89	32.50	32.61	34.92	0.980	0.981	0.981	0.985
VL	36.58	37.55	38.98	39.23	0.994	0.987	0.996	0.995
TN	33.59	35.92	36.05	37.35	0.989	0.991	0.992	0.995
SL	40.72	40.12	41.23	42.19	0.998	0.994	0.997	0.998

③ Likewise, we observe the significant impact of the perceptual loss that we included in the training of neural networks, resulting in an improvement of 1.1 dB in PSNR. These findings remain consistent for SSIM as well. This underscores the effectiveness of incorporating perceptual loss in improving both pixel-level fidelity and structural similarity in the reconstructed frames.

## 6.6 Latency of *PatchEX*

As mentioned in Section 4, we divide *PatchEX* into five major steps. The runtime latency of these steps is shown in Table 12. We make the following observations from the table:

① Due to the partitioning of the frame and parallelization of the extrapolation processes, the inference latency is impressively low. Specifically, for 360p resolution, the latency is merely 0.67 ms. Even for higher resolutions such as 1080p, the latency remains remarkably low, averaging only about 2 ms.

② For other components, such as warping and preprocessing, the latency tends to increase as the frame resolution increases.

Table 12. Runtime (ms) breakdown of the proposed method at various resolution levels

Scenes	Step				
	G-Buffer	Warping	Preprocessing	Inference	Blending
360p	0.17	0.75	1.44	0.67	0.01
480p	0.36	0.89	1.89	1.28	0.01
720p	1.01	1.58	2.19	1.98	0.02
1080p	1.21	2.05	3.12	2.14	0.03

## 7 CONCLUSION

With high-frequency displays becoming increasingly popular, generating frames for real-time applications at higher rates with superior quality is necessary. Since applications are very demanding in terms of processing power, even most GPUs cannot provide a consistently high frame rate at an HD/4K resolution. This work illustrates one such method, *PatchEX*, of supersampling in the temporal domain that strives to provide the quality of interpolation with the latency of extrapolation. We propose a novel method of partitioning the frame into patches and parallelizing the extrapolation tasks of these patches to reduce the latency of the temporal supersampling task. Furthermore, to improve the quality of the final extrapolated frame, we propose using different types of extrapolation algorithms using our bespoke neural networks for each patch. We also recognize the importance of computing shadows correctly, extrapolating them and blending them into the final output. We achieved an improvement of 48.46% in quality (PSNR) and 2× better latency as compared to the nearest competing work.

## REFERENCES

2023. Gaming Monitors Market Trend, Share, Growth, Size and Forecast 2030. <https://www.zionmarketresearch.com/report/gaming-monitors-market-size>. [Online; accessed 2024-05-15].
2024. Mixamo. <https://www.mixamo.com/>. [Online; accessed 2024-04-10].
- Mohammad Alja'afreh. 2021. *A QoE Model for Digital Twin Systems in the Era of the Tactile Internet*. Ph. D. Dissertation. Université d'Ottawa/University of Ottawa.
- Dmitry Andreev. 2010. Real-time frame rate up-conversion for video games: or how to get from 30 to 60 fps for "free". In *ACM SIGGRAPH 2010 Talks*. ACM, LA, USA, 1–1.
- Anonymous Authors. 2024. Video Results. [https://drive.google.com/drive/folders/1hfo7vzAFXd3SzJ0MbtLXpD\\_TnvTTsc9K](https://drive.google.com/drive/folders/1hfo7vzAFXd3SzJ0MbtLXpD_TnvTTsc9K). [Online; accessed 2024-06-12].
- Yash Belhe, Michaël Gharbi, Matthew Fisher, Iliyan Georgiev, Ravi Ramamoorthi, and Tzu-Mao Li. 2023. Discontinuity-Aware 2D Neural Fields. *ACM Transactions on Graphics (TOG)* 42, 6 (2023), 1–11.
- Marcelo Bertalmio, Guillermo Sapiro, Vincent Caselles, and Coloma Ballester. 2000. Image inpainting. In *Proceedings of the 27th annual conference on Computer graphics and interactive techniques*. 417–424.
- Mårten Björkman and Jan-Olof Eklundh. 2005. Foveated figure-ground segmentation and its role in recognition. In *2005 16th British Machine Vision Conference, BMVC 2005, Oxford, United Kingdom, 5 September 2005 through 8 September 2005*. British Machine Vision Association, BMVA, Oxford, United Kingdom, 819–828.
- Thierry Bouwmans, Caroline Silva, Cristina Marghes, Mohammed Sami Zitouni, Harish Bhaskar, and Carl Frelicot. 2018. On the role and the importance of features for background modeling and foreground detection. *Computer Science Review* 28 (2018), 26–91.
- Huw Bowles, Kenny Mitchell, Robert W Sumner, Jeremy Moore, and Markus Gross. 2012. Iterative image warping. In *Computer graphics forum*, Vol. 31. Wiley Online Library, 237–246.
- Andrew Burnes and Henry C Lin. 2023. NVIDIA ADA Science. <https://images.nvidia.com/aem-dam/Solutions/geforce/ada/ada-lovelace-architecture/nvidia-ada-gpu-science.pdf>. [Online; accessed 2023-05-09].

- Ugur Demir and Gozde Unal. 2018. Patch-based image inpainting with generative adversarial networks. *arXiv preprint arXiv:1803.07422* (2018).
- Gyorgy Denes, Akshay Jindal, Aliaksei Mikhailiuk, and Rafal K Mantiuk. 2020. A perceptual model of motion quality for rendering with adaptive refresh-rate and resolution. *ACM Transactions on Graphics (TOG)* 39, 4 (2020), 133–1.
- Gunnar Farneback. 2003. Two-frame motion estimation based on polynomial expansion. In *Image Analysis: 13th Scandinavian Conference, SCIA 2003 Halmstad, Sweden, June 29–July 2, 2003 Proceedings 13*. Springer, 363–370.
- Suzette Fernandes and Monica S Castelhana. 2021. The foreground bias: Initial scene representations across the depth plane. *Psychological Science* 32, 6 (2021), 890–902.
- Epic Games. 2023a. Marketplace. <https://www.unrealengine.com/marketplace/en-US/store>. [Online; accessed 2023-05-23].
- Epic Games. 2023b. Unreal Engine 5. <https://www.unrealengine.com/en-US/unreal-engine-5>. [Online; accessed 2024-04-10].
- Felix Gemblar, Piotr Stawicki, Aya Rezeika, Abdul Saboor, Mihaly Benda, and Ivan Volosyak. 2018. Effects of monitor refresh rates on c-VEP BCIs. In *Symbiotic Interaction: 6th International Workshop, Symbiotic 2017, Eindhoven, The Netherlands, December 18–19, 2017, Revised Selected Papers 6*. Springer, 53–62.
- Brian Guenter, Mark Finch, Steven Drucker, Desney Tan, and John Snyder. 2012. Foveated 3D graphics. *ACM Trans. Graph.* 31, 6, Article 164 (nov 2012), 10 pages. <https://doi.org/10.1145/2366145.2366183>
- Christine Guillemot and Olivier Le Meur. 2013. Image inpainting: Overview and recent advances. *IEEE signal processing magazine* 31, 1 (2013), 127–144.
- Jie Guo, Xihao Fu, Liqiang Lin, Hengjun Ma, Yanwen Guo, Shiqiu Liu, and Ling-Qi Yan. 2021. ExtraNet: real-time extrapolated rendering for low-latency temporal supersampling. *ACM Transactions on Graphics (TOG)* 40, 6 (2021), 1–16.
- Chengcheng Han, Guanghua Xu, Xiaowei Zheng, Peiyuan Tian, Kai Zhang, Wenqiang Yan, Yaguang Jia, and Xiaobi Chen. 2022. Assessing the effect of the refresh rate of a device on various motion stimulation frequencies based on steady-state motion visual evoked potentials. *Frontiers in Neuroscience* 15 (2022), 757679.
- Ruian He, Shili Zhou, Yuqi Sun, Ri Cheng, Weimin Tan, and Bo Yan. 2024. Low-latency Space-time Supersampling for Real-time Rendering. In *Proceedings of the AAAI Conference on Artificial Intelligence*, Vol. 38. AAAI Press, Washington, DC, USA, 2103–2111.
- Robert Herzog, Elmar Eisemann, Karol Myszkowski, and H-P Seidel. 2010. Spatio-temporal upsampling on the GPU. In *Proceedings of the 2010 ACM SIGGRAPH symposium on Interactive 3D Graphics and Games*. ACM, Washington DC, USA, 91–98.
- Juho Pekka Huhti. 2019. The Effect of High Monitor Refresh Rate on Game Experience. (2019).
- Jason Jerald and Mary Whitton. 2009. Relating scene-motion thresholds to latency thresholds for head-mounted displays. (2009), 211–218.
- Jason J Jerald. 2009. *Scene-motion-and latency-perception thresholds for head-mounted displays*. Ph. D. Dissertation. The University of North Carolina at Chapel Hill.
- Justin Johnson, Alexandre Alahi, and Li Fei-Fei. 2016. Perceptual losses for real-time style transfer and super-resolution. In *Computer Vision—ECCV 2016: 14th European Conference, Amsterdam, The Netherlands, October 11–14, 2016, Proceedings, Part II 14*. Springer, Amsterdam, The Netherlands, 694–711.
- Sungkil Lee, Younguk Kim, and Elmar Eisemann. 2018. Iterative depth warping. *ACM Transactions on Graphics (TOG)* 37, 5 (2018), 1–13.
- Liyuan Li, Weimin Huang, Irene Yu-Hua Gu, and Qi Tian. 2004. Statistical modeling of complex backgrounds for foreground object detection. *IEEE Transactions on image processing* 13, 11 (2004), 1459–1472.
- Zhan Li, Carl S Marshall, Deepak S Vembar, and Feng Liu. 2022. Future Frame Synthesis for Fast Monte Carlo Rendering. In *Graphics Interface 2022*. CHCCS, Montreal, Quebec, Canada, 74–83.
- Dongju Liu and Jian Yu. 2009. Otsu method and K-means. In *2009 Ninth International conference on hybrid intelligent systems*, Vol. 1. IEEE, 344–349.
- Shuying Liu and Weihong Deng. 2015. Very deep convolutional neural network based image classification using small training sample size. In *2015 3rd IAPR Asian Conference on Pattern Recognition (ACPR)*. IEEE, Kuala Lumpur, Malaysia, 730–734. <https://doi.org/10.1109/ACPR.2015.7486599>
- Shengmei Liu, Atsuo Kuwahara, James J Scovell, and Mark Claypool. 2023. The effects of frame rate variation on game player quality of experience. In *Proceedings of the 2023 CHI Conference on Human Factors in Computing Systems*. ACM, Hamburg, Germany, 1–10.
- Jiayi Meng, Sibendu Paul, and Y Charlie Hu. 2020b. Coterie: Exploiting frame similarity to enable high-quality multiplayer vr on commodity mobile devices. In *Proceedings of the Twenty-Fifth International Conference on Architectural Support for Programming Languages and Operating Systems*. ACM, Lausanne, Switzerland, 923–937.
- Xiaoxu Meng, Ruofei Du, and Amitabh Varshney. 2020a. Eye-dominance-guided foveated rendering. *IEEE transactions on visualization and computer graphics* 26, 5 (2020), 1972–1980.
- Joerg H Mueller, Philip Voglreiter, Mark Dokter, Thomas Neff, Mina Makar, Markus Steinberger, and Dieter Schmalstieg. 2018. Shading atlas streaming. *ACM Transactions on Graphics (TOG)* 37, 6 (2018), 1–16.
- Koshiro Murakami, Kazuya Miyashita, and Hideo Miyachi. 2021. A Study on the Relationship Between Refresh-Rate of Display and Reaction Time of eSports. In *Advances on P2P, Parallel, Grid, Cloud and Internet Computing: Proceedings of the 15th International Conference on P2P, Parallel, Grid, Cloud and Internet Computing (3PGCIC-2020)* 15. Springer, 339–347.

- Diego Nehab, Pedro V Sander, Jason Lawrence, Natalya Tatarchuk, and John R Isidoro. 2007. Accelerating real-time shading with reverse reprojection caching. In *Graphics hardware*, Vol. 41. ACM, California, USA, 61–62.
- Albert Ng, Julian Lepinski, Daniel Wigdor, Steven Sanders, and Paul Dietz. 2012. Designing for low-latency direct-touch input. In *Proceedings of the 25th annual ACM symposium on User interface software and technology*. ACM, New York, USA, 453–464.
- Simon Niklaus and Feng Liu. 2020. Softmax splatting for video frame interpolation. In *Proceedings of the IEEE/CVF conference on computer vision and pattern recognition*. 5437–5446.
- Avinash Paliwal, Brandon G Nguyen, Andrii Tsarov, and Nima Khademi Kalantari. 2023. ReShader: View-Dependent Highlights for Single Image View-Synthesis. *ACM Transactions on Graphics (TOG)* 42, 6 (2023), 1–9.
- Adam Paszke, Sam Gross, Francisco Massa, Adam Lerer, James Bradbury, Gregory Chanan, Trevor Killeen, Zeming Lin, Natalia Gimelshein, Luca Antiga, et al. 2019. Pytorch: An imperative style, high-performance deep learning library. In *Advances in neural information processing systems*, Vol. 32. NeuRIPS, Vancouver, Canada.
- Cai Ran, Xinfu Li, and Fang Yang. 2023. Multi-Step Structure Image Inpainting Model with Attention Mechanism. *Sensors* 23, 4 (2023). <https://doi.org/10.3390/s23042316>
- Olaf Ronneberger, Philipp Fischer, and Thomas Brox. 2015. U-net: Convolutional networks for biomedical image segmentation. In *Medical image computing and computer-assisted intervention—MICCAI 2015: 18th international conference, Munich, Germany, October 5-9, 2015, proceedings, part III 18*. Springer, Munich, Germany, 234–241.
- Saeed Shafiee Sabet, Steven Schmidt, Saman Zadtootaghaj, Babak Naderi, Carsten Griwodz, and Sebastian Möller. 2020. A latency compensation technique based on game characteristics to mitigate the influence of delay on cloud gaming quality of experience. In *Proceedings of the 11th ACM Multimedia Systems Conference*. ACM, Virtual, 15–25.
- Joi Shimizu, Heming Sun, and Jiro Katto. 2022. Forward and Backward Warping for Optical Flow-Based Frame Interpolation. In *2022 International Conference on Artificial Intelligence in Information and Communication (ICAIIIC)*. IEEE, IEEE, Jeju Island, Korea, 082–086.
- Maria Shugrina, Ziheng Liang, Amlan Kar, Jiaman Li, Angad Singh, Karan Singh, and Sanja Fidler. 2019. Creative flow+ dataset. In *Proceedings of the IEEE/CVF Conference on Computer Vision and Pattern Recognition*. IEEE, California, USA, 5384–5393.
- DELL Technologies. 2023. Alienware 500Hz Gaming Monitor - AW2524HF. <https://www.dell.com/en-us/shop/alienware-500hz-gaming-monitor-aw2524hf/apd/210-bjws/monitors-monitor-accessories>. [Online; accessed 2024-03-21].
- Robert Toth, Jim Nilsson, and Tomas Akenine-Möller. 2016. Comparison of projection methods for rendering virtual reality.. In *High Performance Graphics*. ACM, Dublin, Ireland, 163–171.
- Martin Weier, Michael Stengel, Thorsten Roth, Piotr Didyk, Elmar Eisemann, Martin Eisemann, Steve Grogorick, André Hinkenjann, Ernst Kruijff, Marcus Magnor, et al. 2017. Perception-driven accelerated rendering. *Computer Graphics Forum* 36, 2 (2017), 611–643.
- Songyin Wu, Sungye Kim, Zheng Zeng, Deepak Vembar, Sangeeta Jha, Anton Kaplanyan, and Ling-Qi Yan. 2023a. ExtraSS: A Framework for Joint Spatial Super Sampling and Frame Extrapolation. In *SIGGRAPH Asia 2023 Conference Papers*. ACM, LA, USA, 1–11.
- Zhizhen Wu, Chenyu Zuo, Yuchi Huo, Yazhen Yuan, Yifan Peng, Guiyang Pu, Rui Wang, and Hujun Bao. 2023b. Adaptive recurrent frame prediction with learnable motion vectors. In *SIGGRAPH Asia 2023 Conference Papers*. 1–11.
- Yingen Xiong and Kari Pulli. 2009. Mask-based image blending and its applications on mobile devices. In *MIPPR 2009: Remote Sensing and GIS Data Processing and Other Applications*, Vol. 7498. SPIE, 1066–1073.
- Rui Xu, Minghao Guo, Jiaqi Wang, Xiaoxiao Li, Bolei Zhou, and Chen Change Loy. 2021. Texture memory-augmented deep patch-based image inpainting. *IEEE Transactions on Image Processing* 30 (2021), 9112–9124.
- Xiaokun Xu and Mark Claypool. 2024. User Study-based Models of Game Player Quality of Experience with Frame Display Time Variation. In *Proceedings of the 15th ACM Multimedia Systems Conference*. ACM, Bari, Italy, 210–220.
- Zili Yi, Qiang Tang, Shekoofeh Azizi, Daesik Jang, and Zhan Xu. 2020. Contextual residual aggregation for ultra high-resolution image inpainting. In *Proceedings of the IEEE/CVF conference on computer vision and pattern recognition*. 7508–7517.
- Zheng Zeng, Shiqiu Liu, Jinglei Yang, Lu Wang, and Ling-Qi Yan. 2021. Temporally Reliable Motion Vectors for Real-time Ray Tracing. *Computer Graphics Forum* 40 (2021), 79–90.
- Guozhen Zhang, Yuhan Zhu, Haonan Wang, Youxin Chen, Gangshan Wu, and Limin Wang. 2023. Extracting motion and appearance via inter-frame attention for efficient video frame interpolation. In *Proceedings of the IEEE/CVF Conference on Computer Vision and Pattern Recognition*. 5682–5692.
- YanCi Zhang, XueHui Liu, and EnHua Wu. 2003. Accelerated backward warping. *Journal of Computer Science and Technology* 18, 1 (2003), 48–55.